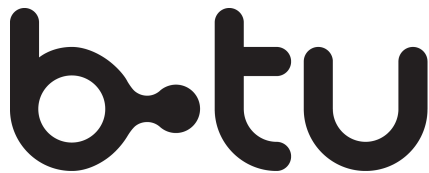


# Electromagnetic Interference and its effects on Acoustic Sensor measurements



Brandenburgische  
Technische Universität  
Cottbus - Senftenberg

*by:*

**Sanjana Rani (B. Tech.)**



Thesis for the degree of Master of Science in  
Transfers-Fluids-Materials in Aeronautical and Space Applications

Chair of Aerodynamics and Fluid Mechanics

**Brandenburg University of Technology, Cottbus–Senftenberg**

Deutsches Zentrum für Luft- und Raumfahrt e.V., **Cottbus, Germany**

15th September, 2024

The copyright of this thesis is owned by the author. Any citations for the thesis or use of any of the information contained in it must acknowledge this thesis as the source of the information.

Author: **Sanjana Rani (B. Tech.)**

████████████████████  
████████████████████  
████████████████████

First Academic Supervisor: *Dr.-Ing. Thomas Geyer*

Chair of Aerodynamics and Fluid Mechanics

AZFD, 2.02

Siemens-Halske-Ring 15a

D-03046 Cottbus, Germany

Second Academic Supervisor: *Dr. Ralf Burgmayer*

Deutsches Zentrum für Luft- und Raumfahrt e. V.

Lieberoser Straße 13a

03046 Cottbus, Germany

## Declaration

In accordance with the appropriate regulations, I hereby submit my thesis and I declare that:

- The report embodies the results of my own work and is composed by myself.
- Where appropriate, I have made acknowledgment of the work of others and have made reference to work carried out in collaboration with other persons.
- The report is the correct version of the report for submission and is the same version as any electronic versions submitted\*.
- I understand that as a student of the University I am required to abide by the Regulations of the University and to conform to its discipline.
- I confirm that the report is entirely written by me, and AI tools like ChatGPT are used for grammar corrections.
- I confirm that the report is verified against plagiarism via an approved plagiarism detection application e.g. Turnitin.
- I declare that the lecturer can submit the electronic copy of the report to a plagiarism detection application e.g. Turnitin.

\* Please note that it is the responsibility of the student to ensure that the correct version of the report is submitted.

Name of the student: **Sanjana Rani (B. Tech.)**

Date: **15 Sep 2024**

Signature of the student:

## Acknowledgements

I would like to thank my supervisors, Dr.-Ing. Thomas Geyer and Dr. Ralf Burgmayer, for their invaluable guidance, experience, and unflinching support during this research journey. Their insightful input, support, and guidance were important in crafting this thesis and advancing my career as a researcher.

I am grateful to Jacob Hurst and Aunanna Rashid for their tremendous help with the experimental setup. Their technical skills and help were critical in overcoming challenges and advancing my research.

My academic endeavors would not have been possible without my parents' unwavering support, encouragement, and sacrifices. I am deeply indebted to them for this. Their belief in me has been a continual source of strength, and I am eternally thankful for their love and guidance.

I also wish to express my heartfelt thanks to my friends in India, France, Belgium, and Germany (BTU and TFM-ASA). Even at such distances, their companionship and encouragement have provided me a great deal of joy and warmth. It has been very helpful to have their compassion and encouraging remarks at difficult times.

Finally, I would want to thank all of the people who have helped me out in different capacities, both seen and unseen. This thesis stands as a testament to your contributions as much as to my own efforts.



## Abstract

The increasing trend of electric propulsion systems in aviation industry demands the development of reliable methods for specifying noise and vibration signatures of new components, such as the electric motor. However, *acoustic sensors* (vital for such measurements) can be susceptible to significant performance degradation due to *Electromagnetic Interference* (EMI) caused by electrified propulsion system. This study is a step towards investigating the application of acoustic sensors for aeroacoustic and vibroacoustics measurements generated by electric motors in electrified aircraft propulsion systems. The research focuses on the impact of EMI on the accuracy of these acoustic measurements obtained through microphones and accelerometers.

The thesis will explore how EMI induces electrical noise in sensor cables and circuits, and analyze the susceptibility of different sensor types to EMI specific to a 5 kW electric motor, depending on various conditions. The results indicate that there was not much impact of EMI on the sensor. The findings indicate minimal EMI effects on sensors for smaller motors under the specific test conditions. The study concludes that further research is required to explore this phenomena in greater depth, potentially using stronger motors.

**Keywords:** electromagnetic interference (EMI), electric-propulsion, acoustic sensors

# Contents

<b>1</b>	<b>Introduction</b>	<b>1</b>
1.1	Background . . . . .	1
1.2	Problem Statement . . . . .	3
1.3	Research Objectives . . . . .	4
1.4	Organization of Report . . . . .	5
<b>2</b>	<b>Fundamentals</b>	<b>6</b>
2.1	EMI . . . . .	6
2.1.1	Classification of EMI . . . . .	6
2.1.2	EMI in motor-drive systems . . . . .	10
2.1.3	EMI in Cables . . . . .	12
2.1.4	EMI Measurement Techniques . . . . .	13
2.1.5	EMI Mitigation Strategies . . . . .	15
2.2	Acoustic Sensors . . . . .	15
2.2.1	Unsteady Pressure Sensors for Aeroacoustics Measurements . . . . .	16
2.2.2	Accelerometers for Vibroacoustic Measurements . . . . .	20
2.3	Signal Processing . . . . .	24
2.3.1	Signal processing Techniques . . . . .	24
<b>3</b>	<b>Materials and Methodology</b>	<b>28</b>
3.1	Research Design . . . . .	28
3.1.1	Purpose . . . . .	28
3.1.2	Approach . . . . .	28
3.2	Materials & Equipment . . . . .	29
3.2.1	Instruments Used . . . . .	29
3.2.2	Test Setup . . . . .	32
3.2.3	Experimental Procedure . . . . .	34
3.3	Data Analysis . . . . .	36
3.3.1	Data Collection & Extraction . . . . .	36
3.3.2	Signal Processing . . . . .	36

<b>4</b>	<b>Results</b>	<b>38</b>
4.1	Acoustic characteristics of the motor . . . . .	38
4.2	Effect of Microphone distance relative to motor . . . . .	40
4.3	Contribution of cable orientation . . . . .	42
4.4	Role of Microphone type . . . . .	44
4.5	Influence of Speaker position . . . . .	45
4.6	Acceleration Sensors . . . . .	48
4.7	Discussion of the results . . . . .	52
4.8	Limitations . . . . .	54
<b>5</b>	<b>Conclusion and Outlook</b>	<b>55</b>
5.1	Conclusion . . . . .	55
5.2	Outlook . . . . .	56
	<b>Appendix A Code Snippets</b>	<b>64</b>

# List of Figures

1.1	Engine noise sources . . . . .	3
2.1	EMI classification based on coupling mechanism . . . . .	7
2.2	EMI classification based on bandwidth of frequency . . . . .	7
2.3	Internal and external sources in Aviation . . . . .	10
2.4	Cable Orientations . . . . .	12
2.5	EMI measurement techniques <sup>[28]</sup> . . . . .	14
2.6	General Working Principle of Microphones . . . . .	16
2.7	Some common types of microphones . . . . .	19
2.8	General working Principle of Accelerometers . . . . .	21
2.9	Schematic diagram of piezoelectric accelerometer . . . . .	21
2.10	Capacitive Accelerometer: (a) The mass is at its resting position when there is no external force. (b) The frame accelerates to the right, when an external force is applied. . . . .	22
2.11	(a) Piezoresistive Accelerometer (b) Triaxial Accelerometer . . . . .	23
3.1	DEWESoft DAQ System . . . . .	30
3.2	Spectrogram . . . . .	32
3.3	Measurement Setup with different speaker positions (black and red represent different types of microphones) . . . . .	33
3.4	Different types of cable orientations . . . . .	34
4.1	Magnitude Spectrum for microphones at $x_0$ with different load conditions . . . . .	39
4.2	Magnitude Spectrum for microphones with different locations relative to the motor . . . . .	41
4.3	Magnitude Spectrum for microphones with different cable orientations . . . . .	42
4.4	Magnitude Spectrum of different type of microphones at $x_3$ . . . . .	44
4.5	Magnitude Spectrum for microphones with different speaker positions relative to the motor . . . . .	46
4.6	Spectral subtraction of microphones closest to the motor . . . . .	47
4.7	Directions of axis relative to motor . . . . .	48

---

4.8	Acceleration of motor in time-domain . . . . .	48
4.9	Normalized Magnitude spectrum of accelerometers at different location . .	49
4.10	Normalized Magnitude spectrum comparison of microphones at $x_3$ and vibration in x & z-axis . . . . .	50
4.11	Coherence of microphone signals at $x_3$ and vibrations in x & z-axis . . . .	52

# List of Tables

1.1	Aircraft Propulsion Systems Comparison . . . . .	2
2.1	Natural and man-made sources of EMI with reference to aircraft . . . . .	9
3.1	DEWESoft Channel Setup . . . . .	31
3.2	Measurement Matrix . . . . .	35
3.3	Motor Specifications . . . . .	35
3.4	Setup Data . . . . .	36

संकट कटै मिटै सब पीरा ॥  
जो सुमिरै हनुमत बलबीरा ॥

All troubles are eradicated, and all pains disappear for those who remember the brave  
and powerful Hanuman.

# 1

## Introduction

### 1.1 Background

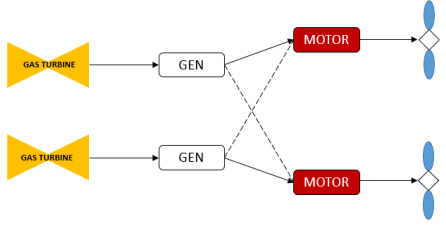
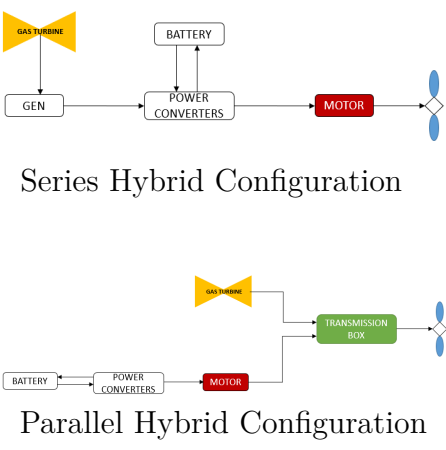
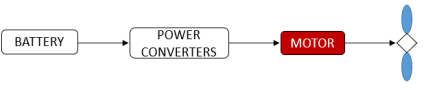
The aviation sector is undergoing significant transformation as it struggles with environmental and technological challenges. Currently, aviation is responsible for 2.4 % of total fuel consumption in the transport sector, contributing to greenhouse gas emissions, global warming, and air pollution <sup>[1]</sup>, which necessitates a significant improvement in propulsion systems. There are several ongoing projects to tackle these environmental impacts. Electric propulsion systems are being seriously considered as one of these revolutionary design concepts. Electric aviation can reduce the environmental footprint of air transport, supporting the EU ACARE [Flightpath 2050](#) emission reduction goals <sup>[2]</sup>.

Electric propulsion systems, particularly plug-in hybrid models, demonstrate high efficiency, with mid-cruise electric propulsion achieving up to 84.7 % efficiency, as demonstrated in the Project [EXACT](#)<sup>[3]</sup>. The EXACT project by DLR aims to explore sustainable aviation technologies to drastically reduce the climate impact of aviation while maintaining economic competitiveness. It examines electric aircraft concepts, energy systems, and air traffic, focusing on designs for 2040 and beyond. The push for sustainable aviation is driven by regulatory pressures, consumer environmental awareness, and industry stakeholders. Airlines are adopting carbon offset programs and investing in greener technologies to meet evolving expectations. Furthermore, electric propulsion systems promise economic benefits, including lower operating and maintenance costs compared to traditional engines, and potential tax incentives. This transition not only addresses environmental and economic concerns but also drives technological advancements in related



fields such as battery technology, power electronics, and electric motor design.

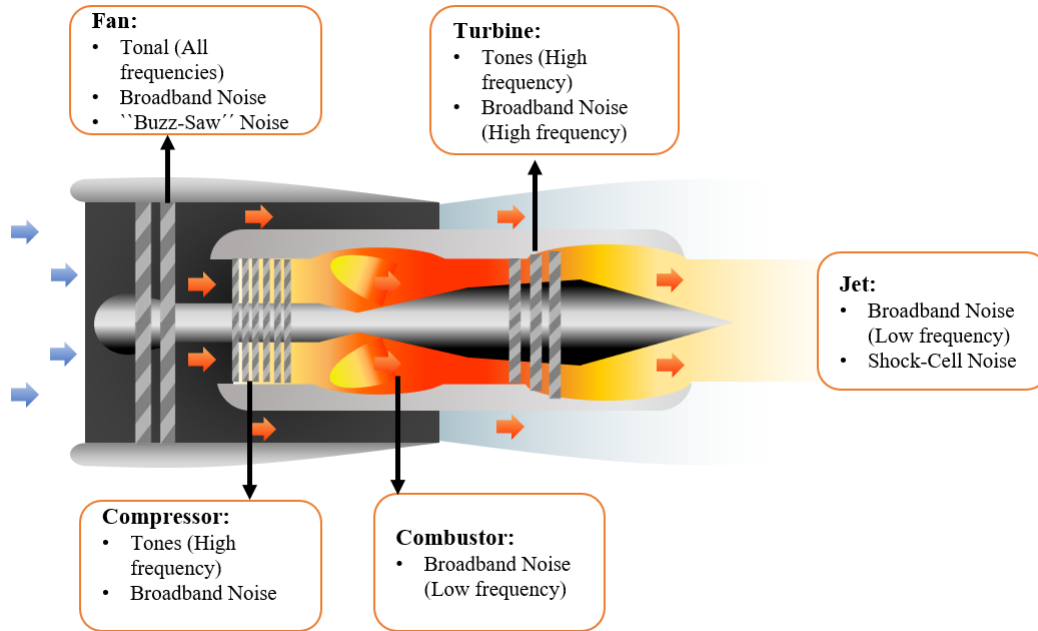
Additionally, electrification also enables capabilities such as electrical vertical take-off and landing (e-VTOL)<sup>[4]</sup> and reduced emissions, making it suitable for regional and short-range aircraft. These electric aircraft can be classified based on their powertrain topology into turboelectric, hybrid-electric propulsion (HEP), and all-electric systems as summarized in Table 1.1<sup>[4][5]</sup>.

Aircraft Propulsion System	Hybridization	Schematic Diagram
<b>Turbo-Electric</b>	One or more gas turbines drive an electric generator to produce electrical power. No energy storage devices (batteries)	
<b>Hybrid-Electric</b>	<p>Uses both gas turbine engines and batteries for propulsion.</p> <ul style="list-style-type: none"> <li>In a series-hybrid configuration, the gas turbine is decoupled from the propeller, and the propeller shaft is driven only by the electric motor.</li> <li>In a parallel-hybrid configuration, the gas turbine engine and the electric motor are connected through a mechanical coupling to the propeller, enabling both powertrains to contribute to the propulsion energy simultaneously or separately</li> </ul>	 <p>Series Hybrid Configuration</p> <p>Parallel Hybrid Configuration</p>
<b>All-Electric</b>	Propulsive power is produced only by batteries.	

**Table 1.1:** Aircraft Propulsion Systems Comparison

Despite the environmental benefits, the transition to electric propulsion systems introduces significant technological challenges, especially in terms of noise and vibration. The

main source of aviation noise is in the engine<sup>[6][7][8]</sup>. There are significant sources of noise in the fan or compressor, combustor, turbine and exhaust jet, explained in figure 1.1.



**Figure 1.1:** Engine noise sources

It is evident from Table 1.1, that all kind of electric propulsion systems have an electric motor. Electric motors in these systems generate electromagnetic, aerodynamic and mechanical noise<sup>[7][9]</sup>, which add to the existing noise sources in aircraft. Electromagnetic noise, also known as electrical noise, is primarily caused by the magnetic field interactions in the air gap between the rotor and the stator of electric motors<sup>[10]</sup>. This noise is generally tonal, resulting from the oscillatory behaviour of the rotating components at specific frequencies.

## 1.2 Problem Statement

Aviation noise, characterized by both tonal<sup>1</sup> and broadband<sup>2</sup> components, can disrupt communities near airports and negatively impact residents' health through stress-mediated disorders such as sleep disturbances and cardiovascular problems<sup>[11]</sup>. Therefore, accurately

<sup>1</sup>Tonal noise is characterized by its periodic nature, with energy concentrated at specific frequencies, manifesting as a distinct pitch or tone.

<sup>2</sup>Broadband noise is characterized by its random and continuous distribution across a wide range of frequencies, arising from turbulent interactions and other random processes.

measuring noise pollution due to aviation is important because it helps regulatory bodies enforce noise control measures, supports the development of quieter aircraft technologies, and ensures compliance with environmental standards, ultimately contributing to more sustainable and community-friendly aviation.

Electric aviation, while offering significant environmental benefits, introduces a new challenge in the form of electromagnetic interference (EMI). There are several sources of EMI in aviation (discussed in section 2.1.1), however, this paper is only focused on the man-made sources of EMI in aviation, specifically motor-drive systems. While electric motors generally operate more quietly, the high-frequency noise they generate, particularly from electromagnetic fields and cooling fans, can create new acoustic challenges.

Acoustic sensors are essential for monitoring and analysing noise sources in aviation. These sensors, mounted on the fuselage of an aircraft, measure both interior and exterior noise, helping in the design of quieter airplanes and reducing noise pollution around airports<sup>[12]</sup>. Different types of sensors are used to capture specific data: unsteady pressure sensors measure acoustic noise levels, while accelerometers measure vibrations. It is important to note that accelerometers do not measure acoustics directly; instead, they detect vibrations, which can cause physical damage to structures and generate noise. However, the performance of these sensors is susceptible to EMI. EMI can distort sensor signals, reduce sensitivity, cause offset drift, induce crosstalk, or even result in complete signal loss<sup>[13]</sup>. Ensuring electromagnetic compatibility (EMC) is crucial for the reliable operation of these sensors in the presence of electric propulsion systems. The challenge lies in the fact that as aircraft become increasingly electrified, the sources and intensity of EMI grow, potentially compromising the integrity of acoustic measurements.

### 1.3 Research Objectives

The primary objective of this study is to evaluate how the electromagnetic fields generated by electric aviation propulsion systems impact the performance of acoustic sensors. The research focuses on understanding the extent of signal distortion due to EMI. By analyzing these interactions, the research seeks to identify the extent of EMI's effects and its implications for noise monitoring in electric aircraft.

To achieve these objectives, the research was conducted both through theoretical and experimental measurements at the German Aerospace Center (DLR) Institute of Flight

Systems in Braunschweig. The study was funded in the scope of the Project **LU(FT)<sup>2</sup>** to comprehend the extent to which acoustic sensors in the vicinity of the electric motor can perform acoustic measurements. The LU(FT)<sup>2</sup> 2030 project focuses on sustainable noise reduction in medium-range aircraft, addressing the issue of aircraft noise. The goal is to make quieter aircraft designs and apply practical noise mitigation strategies.

## 1.4 Organization of Report

This report is structured into the following seven chapters:

1. **Introduction**: Outlines the motivation, problem statement, objectives, and scope of the study.
2. **Fundamentals**: Explains EMI, its sources in aviation, measurement and mitigation techniques. Additionally, it discusses types of acoustic sensors and their vulnerabilities to EMI. Various types of signal processing techniques are explained too.
3. **Materials & Methodology**: Illustrates the overall process of the study and describes the experimental setup.
4. **Results**: Analyses the impact of EMI on acoustic sensor performance and evaluates mitigation strategies.
5. **Conclusion and Outlook**: Summarizes findings, proposes guidelines, and suggests future research directions.

# 2

## Fundamentals

### 2.1 EMI

Electromagnetic Interference (EMI) refers to the unwanted noise/disturbance in electric circuits generated through electromagnetic induction, electrostatic coupling, radiation or conduction causing signal degradation, data corruption, malfunction of electronic devices or complete failure in some cases. EMI can be caused by various sources such as power lines, electric motors, electronic devices (computers or smartphones), radio frequency transmitters or cosmic radiations (lightning) <sup>[14]</sup>.

#### 2.1.1 Classification of EMI

##### Based on EMI coupling mechanisms

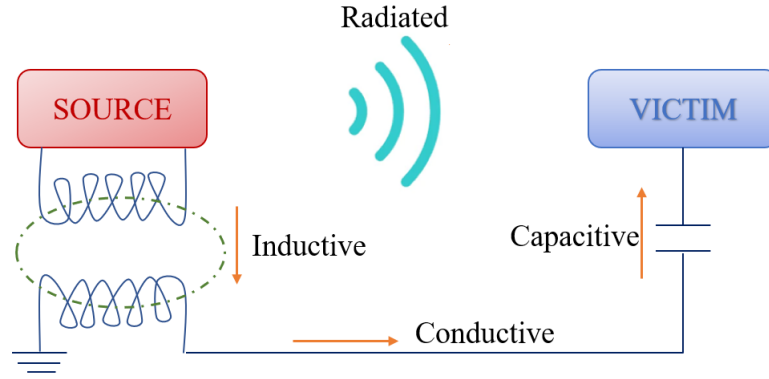
EMI can be categorized based on the coupling mechanism or transmission mode through which it impacts electrical circuits<sup>[15][16]</sup>. Figure 2.1 illustrates the various coupling mechanisms.

1. **Conductive EMI coupling:** This coupling occurs through direct physical contact or conductive mediums, such as power supply lines or communication cables. It is common in situations where electrical noise from one device is transmitted to another through shared conductive pathways. Conduction can happen in two modes,<sup>[14]</sup> *common-mode (CM)* and *differential-mode (DM) currents*.<sup>1</sup>

---

<sup>1</sup>DM currents are equal in magnitude but oppositely directed, with equal and opposite phases. CM currents are equal in magnitude and direction, sharing the same phase relative to ground.

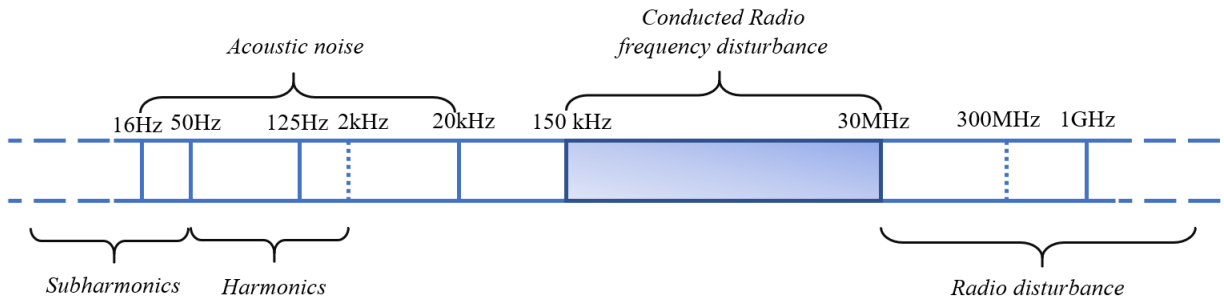
2. **Radiated EMI coupling:** This coupling happens when electromagnetic radiation emitted by one electrical circuit spreads through space and affects nearby circuits. This type of EMI is common in systems with high-frequency signals, like radio communications and wireless devices.



**Figure 2.1:** EMI classification based on coupling mechanism

### Based on bandwidth of frequency

Lasylo Tihanyi [17] classified the electromagnetic disturbances on basis of their frequency content. Figure 2.2 illustrates the classification of electromagnetic disturbances by frequency content.



**Figure 2.2:** EMI classification based on bandwidth of frequency

In [17], electromagnetic signals are differentiated into broadband and narrowband categories under certain conditions which can be expressed mathematically as well. An electromagnetic emission is broadband if:

$$\left| 20 \log \frac{a(f_0)}{a(f_0)2B_i} \right| < 3, \quad (2.1)$$

where  $a(f_0) = \frac{a(\omega)}{2\pi}$  is the amplitude density function

$$a(\omega) = \left| \int_{-\infty}^{\infty} f(t)e^{-j\omega t} dt \right|, \quad (2.2)$$

$f_0$  = center of the measuring bandwidth

$\omega = 2\pi f_0$  = angular frequency

$B_i$  = bandwidth of signal

Equation 2.1 suggests that if the power density over a certain bandwidth  $B_i$  is such that the value of the logarithmic expression is less than 3 dB, the signal is classified as broadband. This is because broadband signals have relatively flat power distribution over a wide range of frequencies, leading to the condition where  $a(f_0)^2 B_i$  remains high in relation to  $a(f_0)$ , making the logarithmic term smaller. If this condition is not met, the signal is classified as narrowband. Narrowband signals concentrate their power within a specific, narrow frequency range, leading to a higher ratio of  $a(f_0)$  relative to  $a(f_0)^2 B_i$ .

### Based on Parasitics

Parasitics refers to undesirable components or effects that accompany the intended electrical behavior of a circuit<sup>[18]</sup>. These parasitic elements arise from the physical properties and layout of components and conductors. The EMI classification based on parasitics is explained in figure 2.1.

1. *Capacitive EMI*: Capacitive coupling occurs when signals are transferred through the capacitance between two closely spaced conductors. Capacitive coupling can induce unwanted voltages and currents in nearby circuits, leading to erroneous behaviour and signal distortion.
2. *Inductive EMI*: Inductive coupling occurs when a current flowing through one conductor induces a voltage in a nearby conductor through its magnetic field. This type of EMI is often seen in systems with high current flows or strong magnetic fields, such as in electric motors and transformers.

### Sources of EMI in Aviation

In [16][19], the authors mention that the EMI experienced by aerospace vehicles can be classified into two basic categories namely: natural and man-made which are listed in Table 2.1

Natural Sources		Man-made Sources	
Terrestrial	Celestial	Systems	Circuits and components
Natural lightning, thunderstorms	Solar Flares, Cosmic Radiation	Communication, radar, navigation, electronic warfare, in-flight-entertainment	Local oscillators, switches, motors, filters, strobe lights, actuators, latching contacts, digital circuits, heaters, pumps

**Table 2.1:** Natural and man-made sources of EMI with reference to aircraft

EMI in aviation can originate from both internal and external sources, see figure 2.3<sup>[19]</sup>:

### 1. Internal Sources

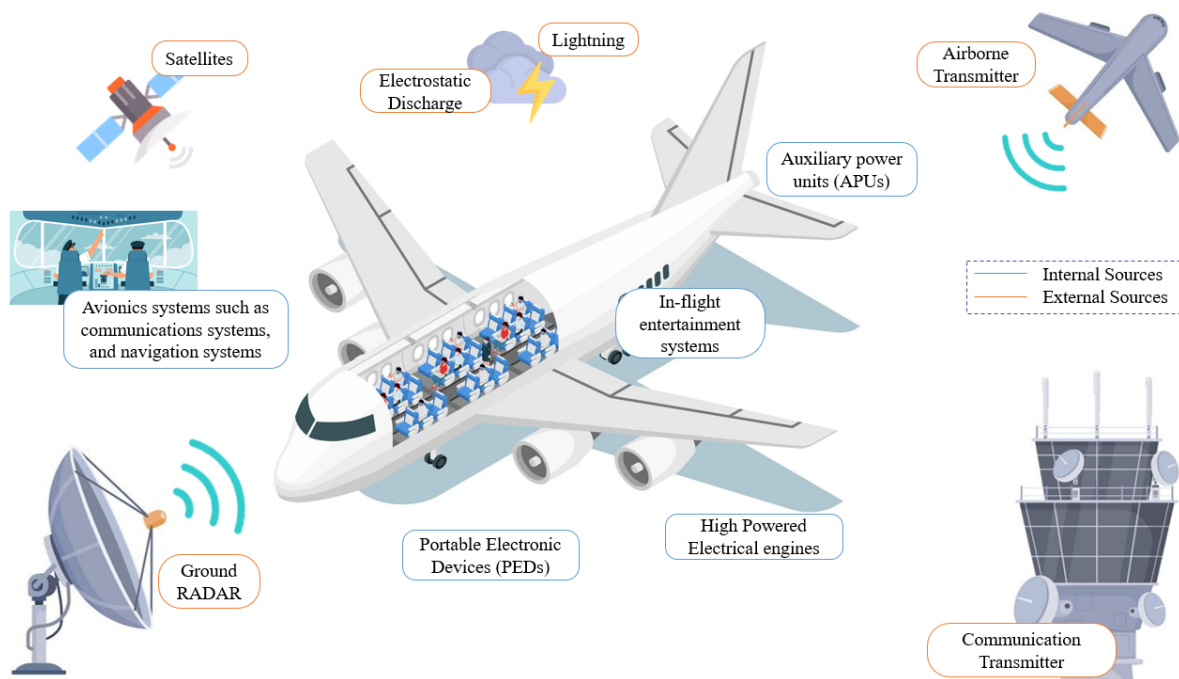
- (a) Avionics Systems: Systems like radios, transponders, GPS, and Instrument Landing System (ILS) emit electromagnetic signals that could disrupt other onboard systems if not properly shielded.
- (b) High-Powered Electrical Systems: Engines, auxiliary power units (APUs), wiring, and motors generate EMI due to high current flows and strong magnetic fields.
- (c) In-Flight Entertainment Systems: Screens, speakers, and wireless communication systems for passenger use can interfere with avionics if not properly shielded.
- (d) Portable Electronic Devices (PEDs): Devices like laptops, tablets, and smartphones emit electromagnetic waves that could pose risks during critical flight phases.
- (e) Environmental Control Systems: Systems such as HVAC and lighting onboard can also be sources of EMI.

### 2. External Sources

- (a) Natural Lightning: Lightning generates intense electromagnetic fields that can disrupt communication and navigation systems.
- (b) Solar Flares and Cosmic Radiation: These phenomena emit significant electromagnetic radiation that can affect aircraft systems.



- (c) Radar Systems and Communication Towers: Emit strong electromagnetic signals that may cause unintended interference.
- (d) Nearby Aircraft: Electronic systems from nearby aircraft can cause interference, especially in congested airspace.
- (e) Satellites: Communication and GPS satellites emit electromagnetic waves that could disrupt aircraft systems.
- (f) Electronic Warfare Systems: Military systems designed to disrupt signals can impact civil aircraft operations.



**Figure 2.3:** Internal and external sources in Aviation

### 2.1.2 EMI in motor-drive systems

Maxwell forces, including attraction and repulsion between magnets and Laplace forces acting on electric currents in external magnetic fields, contribute to EMI in electric motors by causing vibrations in the windings and core of the motor<sup>[10]</sup>. **DC motors** generate rotational motion, which can be converted to translational motion using gears or belts. They operate with stationary windings on the stator and rotating coils on the rotor, where a commutator switches current to the rotor coils, aligning or repelling stator poles. Carbon brushes contact the commutator, leading to high-frequency arcing due to current interruptions, which can create radiated emissions in the 200 MHz to 1 GHz range. To

suppress this, resistors or capacitors may be added. Driver circuits in motors change the rotation direction and provide paths for common-mode currents through connection wires, leading to high-frequency spikes that radiate EMI. Common-mode chokes can block these currents, reducing interference<sup>[14]</sup>. **Stepper motors**<sup>[14]</sup>, despite lacking commutator arcing, face common-mode current issues between driver circuit wires and the motor frame, which is connected for cooling. **AC motors**<sup>[14]</sup>, with closely spaced inductors in the rotor and stator, have large parasitic capacitances that cause common-mode currents to couple from the AC power source to the product frame and vice versa, enhancing radiated or conducted emissions. Common-mode chokes in the attachment leads can block these currents.

The motor drive system used in the experiment, see Chapter 3, is a **permanent magnet synchronous motor (PMSM)** driven by a pulse-width modulation (PWM) Inverter. PMSM are mostly adopted due to their high power density, lower cost and adjustable speed drive (ASD) system<sup>[20]</sup>. There are lots of parasitic and stray parameters in the PMSM drive system. Yingzhe Wu et al.<sup>[20]</sup> stated that the propagation paths of the conducted EMI are formed by the stray capacitances and inductances present in PMSM, which can induce CM currents or DM currents to the equipment. High frequency (HF) impedance characteristic of the motor, including the CM and DM impedances, significantly impacts the level of the conducted EMI in the ASD system.

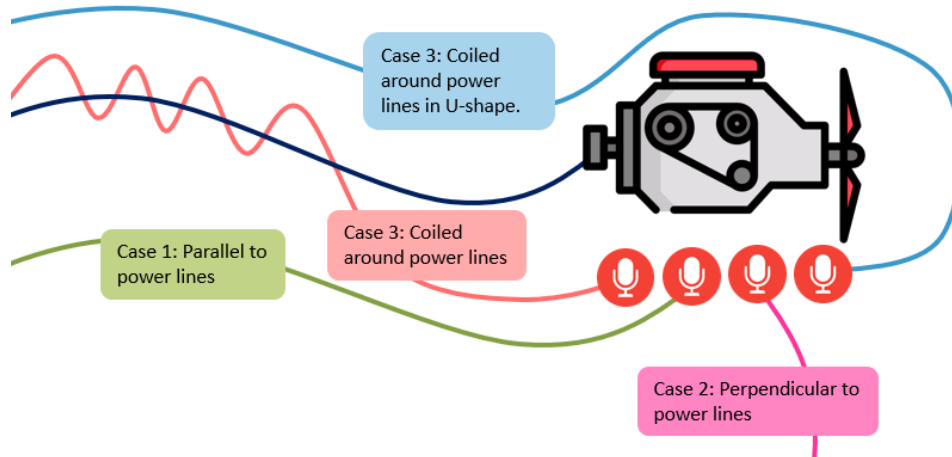
Vijayraghavan et al.<sup>[21]</sup> explained that the machine whose supply voltages are far from sinusoidal, use inverter drive systems producing more harmonic distortions. If the frequencies are close to the natural frequencies of the stator, the forces at these values are high enough to cause considerable electronic noise. EMI can originate from the high-frequency switching operations in **PWM inverters**, leading to high levels of conducted and radiated emissions<sup>[22]</sup>. These switching operations generate substantial electromagnetic emissions that can interfere with both the motor and other nearby electronic systems. The study emphasizes that EMI can cause issues such as increased noise, instability in control systems, and potential degradation of motor components due to parasitic currents induced in motor bearings. J. Adabi et al.<sup>[23]</sup> explained that increasing switching frequency in motor drive systems improves the quality of current waveforms but also produces a high voltage change  $dV/dt$  across the motor terminal due to short switching time. The study revealed that high  $dV/dt$  and common mode voltage generated by PWM inverter in high frequency applications can cause leakage currents, conductive and radiated emissions.

C. Jettanasen and others<sup>[24]</sup> analysed **conducted EMI noise**, which is principally generated by PWM inverter-fed AC motor drive. The simulations and measurements

demonstrate that CM conducted noise is the predominant form of EMI in these systems, exceeding the limits set by standards like DO-160D. This noise is mainly caused by high  $dv/dt$  (voltage) and  $di/dt$  (current) from the fast switching of semiconductor devices such as IGBTs. The presence of parasitic capacitances and inductances across various components, such as between the inverter and ground, leads to unintentional EMI emissions that increase significantly with faster switching and higher parasitic values.

Youpeng Huangfu and others<sup>[25]</sup> focused on the *radiated EMI* generated by an ultra-precision pulsewidth modulation PMSM drive system. The radiated EMI is largely generated by CM ground currents at the output terminal of the converter, which act as excitations for the radiated EMI model. High-frequency switching from the PWM inverter introduces significant harmonic components in the CM current, contributing to the radiated EMI. The spectrum of these currents shows a high number of harmonics at higher frequencies, influencing the EMI radiation in the surrounding environment. The study analyzed radiated EMI in the frequency range from 100 kHz to 40 MHz, with significant interference peaks at certain frequencies caused by the PWM inverter's switching operation.

### 2.1.3 EMI in Cables



**Figure 2.4:** Cable Orientations

The orientation of cables relative to sources of EMI is a critical factor in determining the level of interference experienced by electronic systems. *Parallel cable* runs are particularly prone to EMI because they maximize the mutual inductance between the cable and the

interfering source<sup>[26]</sup>. This coupling can result in significant noise in the signal, especially in environments with strong electromagnetic fields. *U-shaped* patterns can sometimes escalate EMI due to the varying distances and angles between different segments of the cable and the source of interference. They can increase inductive and capacitive coupling, leading to higher levels of EMI, particularly in high-frequency environments<sup>[26]</sup>. Orienting cables *perpendicular* to the power lines might show lower effects of EMI. Perpendicular routing can significantly lower the magnitude of induced voltages in the cables, thereby reducing EMI and improving signal integrity<sup>[26]</sup>.

J L Kotny et al. explains that the length of the power cable in adjustable speed drives (ASDs) significantly impacts EMI levels<sup>[27]</sup>. Longer cables cause a shift in the resonance frequency to lower frequency bands, reducing the influence of motor impedance on the overall EMI. For shorter cables, such as 5 meters, motor impedance has a notable effect, but with longer cables, like 30 meters, the cable itself becomes the dominant factor in EMI generation.

#### 2.1.4 EMI Measurement Techniques

Accurate measurement of EMI is crucial for identifying and addressing interference issues as well as ensuring electromagnetic compatibility (EMC). Key measurement techniques (figure 2.5) include:

##### Emission Testing

Emission testing is crucial for identifying unwanted electromagnetic emissions from electronic instruments, which can be either intentional or unintentional. The equipment under test (EUT) is evaluated for both radiated and conducted emissions, using various test setups to measure and analyze these unwanted signals.

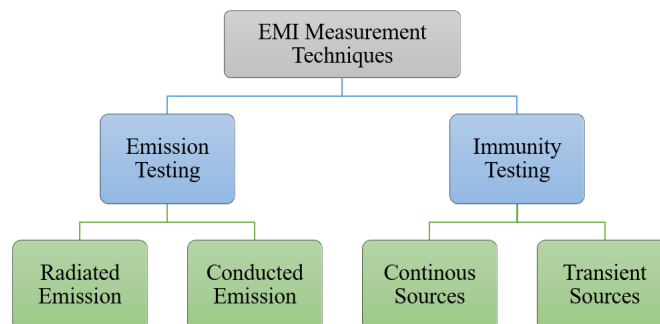
1. **Radiated Emission:** Radiated emissions are measured in an anechoic or semi-anechoic chamber or at an open area test site (OATS)<sup>[28]</sup>. For commercial and industrial products, the frequency range of radiated emission measurements goes from 30 MHz to 6 GHz (CISPR 32) or 30 MHz up to 40 GHz (FCC 47 CFR Part 15)<sup>[29]</sup>. However, the frequency range depends on the industry and may be as wide as from 10 kHz to 40 GHz for defense and military products (MIL-STD-461G)<sup>[29]</sup>.
2. **Conducted Emission:** Conducted emissions are measured at cables that are connected to the equipment under test (EUT)<sup>[28]</sup>. The frequency range of the conducted

emission measurements for commercial and industrial products goes from 150 kHz to 30 MHz (CISPR 32, FCC 47 CFR Part 15)<sup>[29]</sup>. However, the frequency range depends on the industry and may be as wide as from 30 Hz to 40 GHz for defense and military products (MIL-STD-461G)<sup>[29]</sup>.

## Immunity Testing

Immunity testing evaluates how well an EUT can withstand electromagnetic disturbances. It involves exposing the EUT to an electromagnetically hostile environment to observe any changes in its performance.

1. **Continuous Sources:** Continuous immunity testing is aimed at determining if the EUT will function as intended when it is exposed to continuous noise sources such as the solar radiation, broadcast stations or magnetic fields<sup>[28]</sup>. It can be conducted, radiated or magnetic immunity testing. The frequency range of the conducted immunity tests for commercial and industrial products goes from 150 kHz to 80 MHz (IEC 61000-4-6)<sup>[29]</sup>. IEC 61000-4-3 and IEC/EN61000-4-8 are the standards most commonly used for radiated and magnetic field immunity testing respectively<sup>[28]</sup>.
2. **Transient Sources:** Lightning, EM pulses, electrostatic discharge (ESD) and voltage fluctuations are some types of transient sources of EMI which can cause catastrophic effect on system performance<sup>[28]</sup>. IEC 61000-4-2 is the internationally accepted system level standard for immunity testing of an electronic device against ESD and IEC 61000-4-4 is the standard that specifies the setup and method to carry out Electrical Fast Transient/Burst (EFT/B) immunity testing<sup>[29]</sup>.



**Figure 2.5:** EMI measurement techniques<sup>[28]</sup>

### 2.1.5 EMI Mitigation Strategies

Effective EMI mitigation involves various techniques and design considerations to minimize interference <sup>[14]</sup>:

- **Shielding:** It involves enclosing electronic components or systems with conductive or magnetic materials to block or attenuate electromagnetic fields and prevents unwanted EMI to interfere with the device. When the an incident wave interferes on the shield, a major portion is either reflected or absorbed and a small portion gets transmitted. This phenomena is known as *EMI shielding effectiveness (EMI SE)* of the equipment. It is described in equation 2.3<sup>[14][28][29]</sup>:

$$SE = 10 \log \left( \frac{P_{rx}}{P_{rx'}} \right) \text{ dB} \quad (2.3)$$

where  $P_{rx}$  is the power intercepted by the receiver in the absence of shield and  $P_{rx'}$  is the power intercepted by the receiver in presence of shield.

- **Filtering:** This procedure uses filters to attenuate unwanted electromagnetic signals while allowing desired signals through. Filters can be passive (using resistors, capacitors, and inductors), active (utilizing op-amps), or digital (implemented in signal processors)<sup>[30]</sup>. To mitigate EMI, low-pass filters are used to block high-frequency noise from power and signal lines, while common-mode chokes are placed on cables to suppress noise common to both lines. Ferrite beads are clamped around cables to absorb high-frequency interference, improving signal integrity and reducing noise<sup>[14]</sup>. MIL-STD-220 standard specifies a method of measuring the filtering capabilities of passive, low-pass, EMI filters as a function of frequency and considering the influence of temperature and direct current bias<sup>[31]</sup>.
- **Grounding:** It allows unwanted currents to safely dissipate by providing a low-resistance path, thereby reducing EMI. Common methods include earth grounding using rods or plates, chassis grounding for equipment enclosures, and signal grounding to maintain signal integrity<sup>[32]</sup>.

## 2.2 Acoustic Sensors

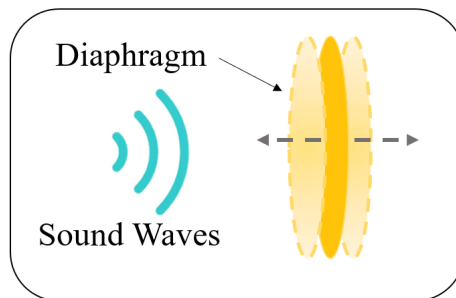
Acoustic sensors are devices that detect sound waves and convert them into electrical signals. These sensors are essential in a wide range of applications, from consumer elec-

tronics and healthcare to industrial and environmental monitoring. This section delves into the fundamental principles, types, and vulnerabilities in acoustic sensor technology.

### 2.2.1 Unsteady Pressure Sensors for Aeroacoustics Measurements

Unsteady pressure sensors are critical tools for aeroacoustics measurements, which involve studying the sound generated by turbulent fluid flows and their interaction with solid boundaries, such as aircraft surfaces. These sensors help in understanding and mitigating noise pollution caused by aircraft and other aerodynamic systems. They are crucial for aircraft noise monitoring, particularly during take-off and landing, where capturing the rapid fluctuations in pressure is essential for understanding and reducing noise pollution. In wind tunnel testing, these sensors measure the aerodynamic forces and noise generated by different airfoil shapes and configurations<sup>[33][34]</sup>.

#### Working principle of Unsteady Pressure Sensors



**Figure 2.6:** General Working Principle of Microphones

In this study, the unsteady pressure sensors used were microphones. Microphones are a type of unsteady pressure sensor that extract sound pressure variations and convert them into electrical signals. They are used in a wide range of applications, including telecommunications, audio recording, and speech recognition. There are several types of microphones, including dynamic microphones, condenser microphones, MEMS microphones and piezoelectric microphones<sup>[35]</sup>. All of them have advantages and disadvantages. However, all of them work on the same basic principle. They include a diaphragm, which is a thin, flexible membrane that vibrates in response to the changes in pressure caused by sound waves. The amplitude and frequency of these vibrations correspond to the characteristics of the sound waves. Conversion of these vibrations is done by the transducer mechanism behind the diaphragm which varies according to the microphone in use.

1. **Piezoelectric Microphones**, also known as *ceramic* or *crystal* microphones, operate on the basis of the so-called piezoelectric effect. These microphones use a piezoelectric crystal as a transducer. The crystal is attached to a diaphragm. When sound waves cause the diaphragm to vibrate, the crystal deforms, generating an electric charge<sup>[35]</sup>. Piezoelectric microphones have typical transmission factors in the range of  $M_0 = 2-20$  mV/Pa<sup>[36]</sup>. The output voltage  $V_a$  is proportional to the pressure  $p$ , as shown in equation 2.4:

$$V_a = \frac{\delta_p S p}{C_0}, \quad (2.4)$$

where

$\delta_p$  = piezoelectric charge coefficient <sup>2</sup>

$S$  = Surface area

$C_0$  = quiescent capacitance <sup>3</sup> (approx. 1-30 nF)

2. **Condenser Microphones**, also known as capacitor microphones, use a capacitor to convert acoustic signals into electrical signals. They consist of a diaphragm and a backplate (capacitor). When sound waves hit the diaphragm, it vibrates, changing the distance between the diaphragm and the backplate, thus varying the capacitance. This change in capacitance leads to a change in voltage at the high-impedance resistor  $R$ . The transmission factor  $M_0$  for condenser microphones is comparatively high at typically  $M_0 > 10$  mV/Pa<sup>[36]</sup>. The condenser principle is based on the equation 2.5

$$Q = CV, \quad (2.5)$$

where  $Q$  is the electrical charge on plates,  $C$  is the capacitance and  $V$  is the applied voltage. The charge is applied either by applying an external polarisation voltage  $V_0$  or by using permanently polarised materials (electrets):

$$(Q_0 + Q_{\sim}) = (C_0 - C_{\sim})(V_0 + V_{\sim}). \quad (2.6)$$

Here,  $C_0$  is the resting capacitance of capacitor,  $C_{\sim}$  is the change in capacitance,  $V_{\sim}$  is the voltage change at resistor and  $Q_{\sim}$  is the change in capacitor charge. Neglecting non-linear terms ( $C_0 \ll C_{\sim}, V_0 \ll V_{\sim}$ )<sup>[36]</sup>, the voltage change  $V_{\sim}$  at the resistor is

$$V_{\sim} = V_0 \frac{C_{\sim}}{C_0} \frac{1}{1 - 1/j\omega RC_0}. \quad (2.7)$$

---

<sup>2</sup>The amount of electric charge generated per unit of applied stress.

<sup>3</sup>The capacitance of a piezoelectric device or capacitor when it is in a state of equilibrium, with no external mechanical stress or electrical signals applied.



So, the resting capacitance  $C_0$  with surface area  $S$ , resting distance  $d_0$  and dielectric constant  $\varepsilon_0\varepsilon_r$  is

$$C_0 = \frac{\varepsilon_0\varepsilon_r S}{d_0}. \quad (2.8)$$

The incoming sound leads to a diaphragm deflection  $\xi$ .

$$C = \frac{C_0}{1 + \xi/d_0}, \quad (2.9)$$

where  $C = (C_0 - C_{\sim})$

For small deflections ( $\xi \ll d_0$ )  $\Rightarrow C \approx C_0(1 - \xi/d_0)$ .

Thus,

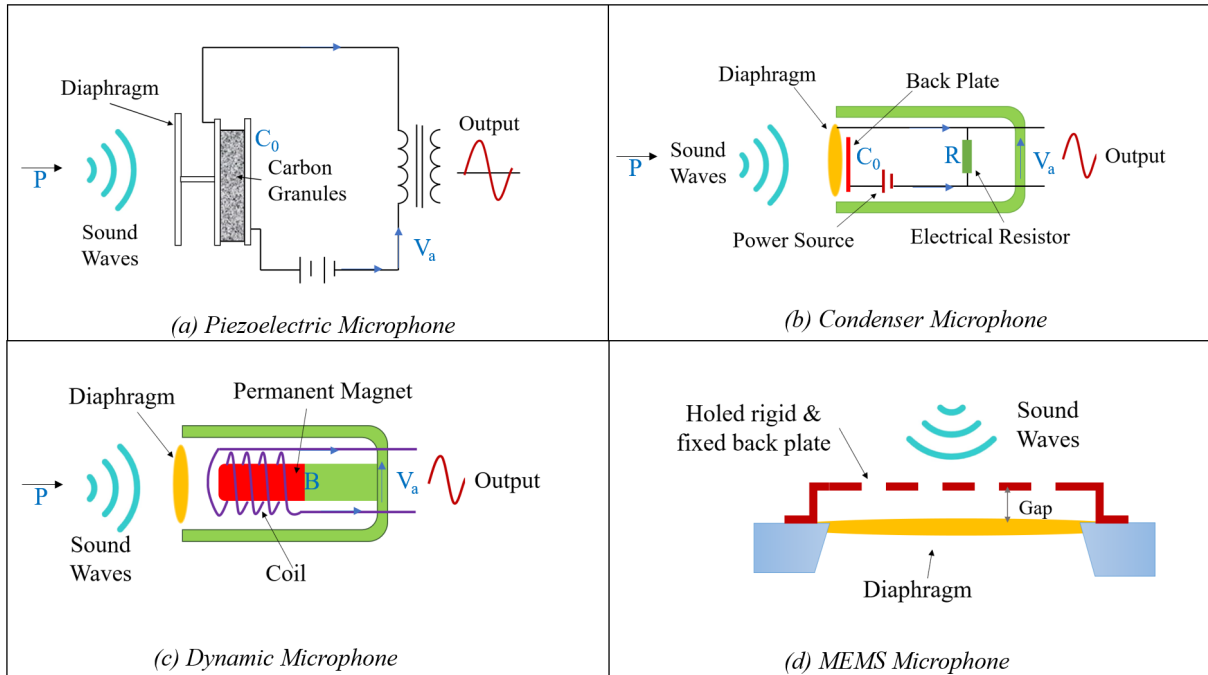
$$V_{\sim} = V_0 \frac{\xi}{d_0}. \quad (2.10)$$

Therefore, equation 2.10 indicates that the output voltage is proportional to the diaphragm movement (deflection receiver).

3. **Dynamic Microphones** work on the principle of electromagnetic induction. A coil of fine wire is attached to a diaphragm placed within the magnetic field of a permanent magnet, therefore known as *moving coil* microphones. When sound waves hit the diaphragm, it vibrates, causing the coil to move within the magnetic field and generate an electrical signal. The transmission factor is comparatively low at around 0.5-2.0 mV/Pa<sup>[36]</sup>. The output voltage  $V_a$  for dynamic microphones (equation 2.11) is proportional to the magnetic flux density  $B$ , the speed  $v$  of the diaphragm movement and length of conductor  $l$ .

$$V_a = Blv \quad (2.11)$$

4. **Micro-Electro-Mechanical Systems (MEMS) Microphones**, also known as microphone chips or silicon microphones, work on MEMS technology. They consist of two conductive plates with the top plate (backplate) being fixed and the bottom plate (diaphragm) able to vibrate when hit by sound waves. This vibration changes the distance between the plates, varying the capacitance, which is then converted into an electrical signal<sup>[35][37]</sup>. MEMS microphones have a transmission factor in range 1-2 mV/Pa and can be higher of about 10 mV/Pa<sup>[38]</sup>.



**Figure 2.7:** Some common types of microphones

### EMI Vulnerability of Microphones

In the paper ‘Detection of Electromagnetic Interference Attacks on Sensor Systems’<sup>[39]</sup>, Youqian Zhang and Kasper Rasmussen investigated the susceptibility of sensor systems, including microphones, to EMI attacks. The study revealed that attackers can inject malicious signals into the analog channels between sensors and microcontrollers, potentially harming the outcomes. The authors proposed a novel detection method to tackle this problem that involved the random modulation of the sensor’s power supply, making it difficult for attackers to predict when the sensor is turned off.

Denis Foo Kune et al.<sup>[40]</sup> addressed the vulnerability of consumer electronics’s microphones to EMI attacks. Their research focused on how low-power EMI can be used to inject malicious signals into microphones by exploiting inadequate filtering in devices. This allows attackers to introduce fake audio signals leading to potential security breaches.

Kasmi and Lopes Esteves<sup>[41]</sup>, explored the sensitivity of smartphone microphones to intentional electromagnetic interference (IEMI) attacks. They demonstrated how headphone cables, acting as unintended antennas, can capture EMI signals. This allows attackers to remotely inject commands through the microphone interface without the user’s knowledge, bypassing user authentication and triggering actions.

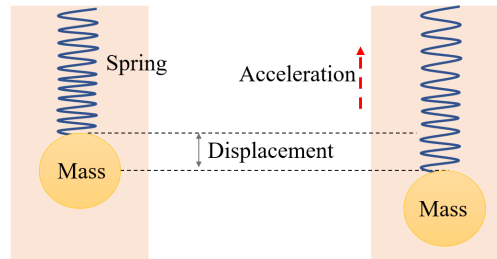
The previous researches targeted the electrical circuits of microphone sensors by intentionally attacking it with EMI to induce some effects and then provide a mitigation technique. However, we initially selected the sensors which might be most susceptible to EMI. Piezoelectric microphones are less impacted by EMI, as their operation is based on mechanical stress rather than electromagnetic properties, but they can still experience interference in environments with strong electromagnetic fields. On the other hand, dynamic microphones are generally more resistant to EMI but can still be affected by strong external magnetic fields<sup>[42]</sup>.

Among the different types of microphones, condenser microphones are the most vulnerable to EMI due to their reliance on stable capacitance. This susceptibility makes them prone to noise and signal distortion in environments with high EMI. MEMS microphones also face significant challenges with EMI because their small size and integrated circuits can easily pick up electromagnetic noise<sup>[43]</sup>. This inherent sensitivity makes them an ideal choice for our study, which aims to understand the impact of EMI on the most susceptible types of microphones. By focusing on condenser microphones, we can gain insights into how EMI affects these sensitive sensors and explore potential mitigation strategies.

## 2.2.2 Accelerometers for Vibroacoustic Measurements

Accelerometers are used to study the vibrations of structures and are vital instruments for vibroacoustic measurements, which involve the study of vibrations and the resulting sound radiation from structures. These measurements are crucial in fields such as structural health monitoring, noise control, and product design. In the aviation industry, accelerometers are used extensively to monitor the vibrations of aircraft components, ensuring the structural integrity of wings, fuselage, and engines<sup>[44]</sup>. They play a critical role in detecting potential issues such as metal fatigue, structural deformations, and component wear and tear, thus enhancing the safety and reliability of aircraft<sup>[45]</sup>. Additionally, accelerometers contribute to noise reduction efforts by identifying and mitigating sources of vibration-induced noise within the aircraft cabin, improving passenger comfort and reducing noise pollution<sup>[46]</sup>.

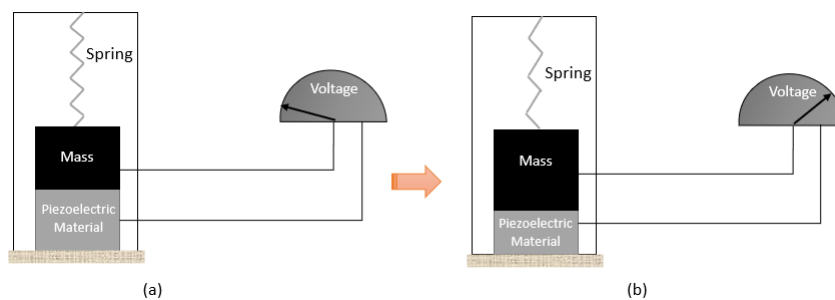
## Working principle of Accelerometers



**Figure 2.8:** General working Principle of Accelerometers

A conventional accelerometer (mechanical accelerometer) works on a spring-mass system. The spring is usually suspended inside an outer casing. When the whole device accelerates, the casing moves off immediately in the same direction. The mass, however, stays at its position (due to inertia), stretching the spring with a force that corresponds to the acceleration<sup>[47]</sup>. Modern accelerometers generate electric or magnetic signals.

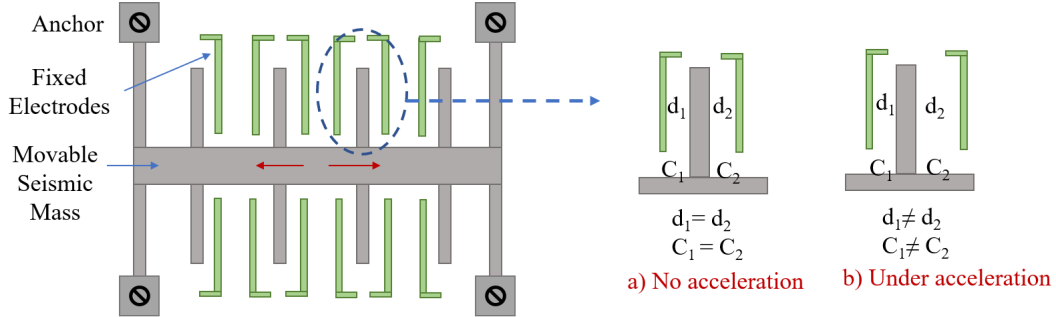
1. **Piezoelectric Accelerometers:** These accelerometers utilize the piezoelectric effect, where certain materials generate an electric charge in response to mechanical stress. The sensor contains a piezoelectric crystal bonded to a mass. When the accelerometer experiences acceleration, the mass exerts a force on the crystal, causing it to deform. This deformation generates an electrical charge proportional to the applied force, which is then measured to determine the acceleration.



**Figure 2.9:** Schematic diagram of piezoelectric accelerometer

2. **Capacitive Accelerometers:** Capacitive accelerometers measure changes in capacitance resulting from the relative motion of internal components. They consist of two conductive plates: one fixed to the sensor body and one attached to a movable mass. When the sensor experiences acceleration, the mass moves relative to

the fixed plate, changing the distance between the plates and thus varying the capacitance. This capacitance change is detected and converted into an acceleration measurement.



**Figure 2.10:** Capacitive Accelerometer: (a) The mass is at its resting position when there is no external force. (b) The frame accelerates to the right, when an external force is applied.

**3. Piezoresistive Accelerometers:** Piezoresistive accelerometers rely on changes in electrical resistance of piezoresistive materials when subjected to mechanical stress. These sensors typically consist of a mass attached to a flexible cantilever beam embedded with piezoresistive elements. When the sensor undergoes acceleration, the mass causes the cantilever beam to bend, inducing stress in the piezoresistive elements. This stress changes their electrical resistance, which is measured and converted into an acceleration value. Lets consider a uniformly stressed cantilever beam of length  $L$ , loaded with mass  $m$  at its end. A piezoresistive accelerometer with resistance  $R$  is cemented to the top of beam (figure 2.11a). A change of length of beam produces a change in resistance of accelerometer. The gage factor  $K$ <sup>4</sup> for the sensor is given by [48] equation 2.12

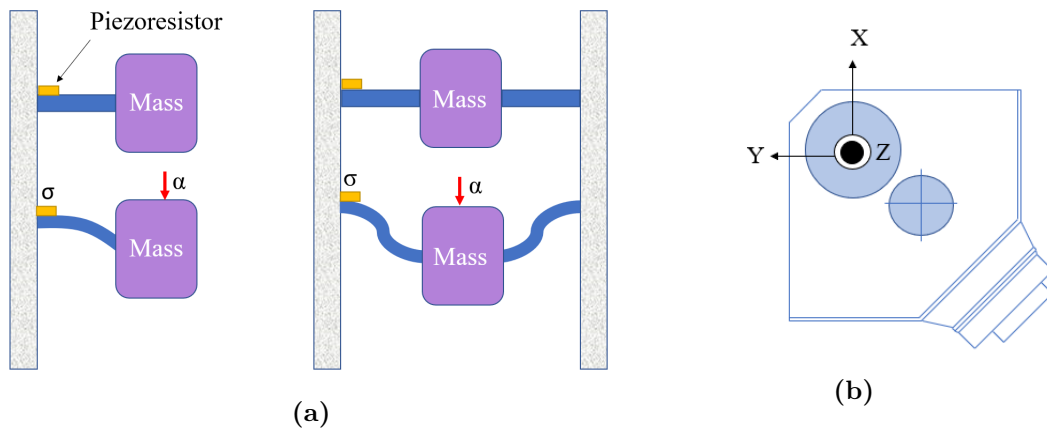
$$K = \frac{\Delta R/R}{\Delta L/L} = \frac{\Delta R/R}{\epsilon} \quad (2.12)$$

where  $\Delta R$  is the resistance change due to strain,  $\Delta L$  is the change in length and  $\epsilon$  is the strain induced in beam, So, the ratio of output voltage  $V_0$  of the circuit to the input voltage  $V_i$  is

$$\frac{V_0}{V_i} = \frac{\Delta R/R}{R} = \epsilon K \quad (2.13)$$

**4. Triaxial Accelerometers:** Triaxial accelerometers are designed to measure acceleration along three perpendicular axes (X, Y, and Z). They can be based on

<sup>4</sup>It measures how the electrical resistance of a material changes with mechanical strain.



**Figure 2.11:** (a) Piezoresistive Accelerometer (b) Triaxial Accelerometer

various sensing principles, such as piezoelectric, piezoresistive, or capacitive mechanisms. Triaxial accelerometers contain three separate sensing elements, each aligned with one of the three axes. When the sensor experiences acceleration, each sensing element independently measures the acceleration along its respective axis.

### EMI Vulnerability of Accelerometers

The paper ‘Review of Intentional Electromagnetic Interference on UAV Sensor Modules and Experimental Study’ by Kim et al.<sup>[49]</sup> examines the effects of IEMI on various sensor modules used in drones, particularly accelerometers and gyroscopes. They used a BiLog antenna<sup>5</sup> with a frequency range of 30 MHz–2 GHz and a typical gain of 6 dB in the chosen frequency range. To increase the effect of IEMI, an amplifier with a gain of 50 dB was used together with the antenna for maximum possible output. The study finds that no changes in sensor data are observed in accelerometers, owing to the insufficient amount of coupling onto the circuit. The reason for this low coupling level is the small dimensions of the target circuit. The researchers addressed this problem by suggesting the use of high-power signals with a wide range of frequencies.

Lubkowski et al.<sup>[51]</sup> investigate the impact of high-power electromagnetic (HPEM) pulses on the sensor systems of unmanned aerial vehicles (UAVs), with a focus on accelerometers. Their study concludes that while accelerometers are generally resilient to direct disturbances from HPEM pulses, their readings can be indirectly affected by rapid variations in UAV motor speeds caused by the interference. This motor instability results in vibrations detected by the accelerometers, leading to minor fluctuations in their readings. Although

<sup>5</sup>The Bilog antenna represents a combination of a biconical antenna and a log-periodic dipole array, both used in EMI measurements<sup>[50]</sup>.

these fluctuations do not exceed typical values observed during normal UAV operations, the findings suggest that while accelerometers are robust against direct HPEM interference, they can still be compromised through induced mechanical vibrations, indicating a potential vulnerability in UAV sensor systems under electromagnetic threats.

Wade A. Smith <sup>[52][53]</sup> focused on the contamination of vibration signals with EMI generated from the pulse-width modulated (PWM) control signals used by variable frequency drives (VFDs). EMI from PWM-based VFDs can be generated from different mechanisms, the major one being large line-to-ground current spikes. In the time-domain signal, these high frequency currents appear in vibration signal as sharp spikes or dropouts spanning perhaps two or three samples, preceded or followed by sawtooth oscillations (at  $\approx 0.4$  times the sampling rate).

Capacitive accelerometers are the most vulnerable to EMI due to their reliance on precise capacitance measurements. External electromagnetic fields can significantly alter these measurements, leading to inaccurate readings. MEMS-based triaxial accelerometers are also prone to EMI, as the integrated circuits used in these devices can pick up electromagnetic noise<sup>[54]</sup>. Piezoelectric accelerometers, while generally more resistant to EMI, can still experience issues in environments with strong electromagnetic fields<sup>[55]</sup>.

## 2.3 Signal Processing

Signal processing involves converting or transforming data in a way that allows us to see things in it that are not possible via direct observation. Signal processing is a field of engineering, mathematics, and computer science that deals with processing, analyzing, and manipulating analog and digital signals. Some common signal-processing tasks include filtering, Fourier analysis, noise reduction, compression, and feature extraction. When analyzing signals or systems, two fundamental domains are often used: the *frequency* domain and the *time* domain.

### 2.3.1 Signal processing Techniques

#### Fourier Transform

The Fourier Transform converts a time-domain signal into a frequency-domain representation. Consider a continuous time signal  $x(t)$ <sup>[56]</sup>. The *Fourier transform* of the signal in

frequency-domain is given as:

$$X(f) = \int_{-\infty}^{\infty} x(t) e^{-j2\pi ft} dt \quad (2.14)$$

1. **Discrete Fourier Transform (DFT):** For a discrete-time signal  $x[n]$ , the DFT is given by:

$$X[k] = \sum_{n=0}^{N-1} x[n] e^{-j2\pi kn/N} \quad (2.15)$$

where  $N$  is the discrete signal samples and  $k$  is the frequency index.

2. **Fast Fourier Transform (FFT):** The DFT as defined in equation 2.15 has a complexity of  $N^2$  complex multiplications and  $N(N - 1)$  complex additions. By decomposing the original  $N$ -point DFT into successively smaller DFTs, the amount of computations can be dramatically reduced<sup>[57]</sup>. The resultant algorithms are collectively known as Fast Fourier Transform (FFT).

## Magnitude Spectrum Analysis

The magnitude spectrum  $A(f)$  is a representation of the magnitude (or absolute value) of the Fourier transform of a signal, as a function of frequency. It provides information about the amplitude of different frequency components present in the signal, without considering their phase. So, the magnitude of FFT signal can be given as:

$$A(f) = |X_f| \quad (2.16)$$

To obtain the amplitude of spectral components, we must divide the absolute value of the spectrum by the number of samples  $N$ , and multiply by two, as the signal energy is divided into two mirrored halves. So, the magnitude of a spectral component at index  $n$  is given by equation 2.17.

$$A[n] = \frac{2}{N} |x[n]| \quad (2.17)$$

## Power Spectrum Analysis

The power spectrum of a signal represents the distribution of power into frequency components composing that signal. The power spectrum  $P(f)$  is the absolute value of spectrum squared.

$$P(f) = |X_f|^2 \quad (2.18)$$



Power Spectral Density  $S(f)$  describes how the power of a signal is distributed across different frequencies.

$$S(f) = \frac{1}{T} \lim_{T \rightarrow \infty} |X(f)|^2 \quad (2.19)$$

Power spectrum gives a direct measure of power at specific frequencies whereas, power spectral density (PSD) provides a normalized measure of power per unit frequency, which is useful for understanding how power varies over a range of frequencies, especially in random signals.

Often, we use logarithmic spectrum, expressed in decibels (dB):

$$A(f) = 10 \cdot \log_{10} |X_f| \quad (2.20)$$

$$P(f) = 10 \cdot \log_{10} |X_f|^2 = 20 \log_{10} |X_f| \quad (2.21)$$

## Coherence

Coherence is used to quantify the degree of linear correlation between two signals. The coherence function, denoted typically as  $C_{xy}(f)$ , is a frequency-domain measure that ranges between 0 and 1. A coherence value close to 1 indicates a strong linear relationship between the signal at the frequency, while a value close to 0 suggests little to no correlation. Coherence is mathematically given by

$$C_{xy}(f) = \frac{|S_{xy}(f)|^2}{S_{xx}(f) S_{yy}(f)} \quad (2.22)$$

where

$S_{xy}(f)$  - Cross Spectral Density<sup>6</sup> of the signals  $x$  and  $y$

$S_{xx}(f)$  - Power Spectral Density of the signals  $x$

$S_{yy}(f)$  - Power Spectral Density of the signals  $y$

## Spectral Subtraction

The so-called Spectral Subtraction is a technique used in signal processing, to improve the quality of a signal by estimating and subtracting the noise component from it. It involves restoration of the power spectrum or the magnitude of a signal through subtraction of an average noise spectrum from the spectrum of the signal with noise<sup>[58][59]</sup>.

---

<sup>6</sup>It provides information on how two signals are correlated as a function of frequency.

Consider  $y(t)$ ,  $x(t)$  and  $n(t)$  as the noisy signal, the original signal and the noise in time-domain, where

$$y(t) = x(t) + n(t) \quad (2.23)$$

Assume that all the signals are windowed<sup>7</sup>. The Fourier transforms of the signals will be  $Y(f)$ ,  $X(f)$  and  $N(f)$ . Therefore, equation 2.23 can be expressed as:

$$Y(f) = X(f) + N(f) \quad (2.24)$$

Hence, the equation describing spectral subtraction can be written as:

$$|\hat{X}(f)|^b = |Y(f)|^b - \alpha \overline{|N(f)|^b} \quad (2.25)$$

where  $|\hat{X}(f)|^b$  is an estimate of the original signal spectrum  $|X(f)|^b$  and  $\overline{|N(f)|^b}$  is time-averaged noise spectra. The parameter  $\alpha$  in Equation 2.25 controls the amount of noise subtracted from the noisy signal. For full noise subtraction,  $\alpha = 1$  and for over-subtraction  $\alpha > 1$ <sup>[58]</sup>.

### 1. Magnitude Spectrum Subtraction

For magnitude spectral subtraction, the exponent  $b = 1$ . Equation 2.25 for magnitude spectrum subtraction can be expressed as:

$$|\hat{X}(f)| = |Y(f)| - \overline{|N(f)|} \quad (2.26)$$

### 2. Power Spectrum Subtraction

For power spectral subtraction, the exponent  $b = 2$ . Equation 2.25 for power spectrum subtraction can be expressed as:

$$|\hat{X}(f)|^2 = |Y(f)|^2 - \overline{|N(f)|^2} \quad (2.27)$$

---

<sup>7</sup>In signal processing, the incoming signal is divided into segments of  $N$  samples length. Each segment is windowed, using a Hanning or a Hamming window, and then transformed into  $N$  spectral samples. The windows alleviate the effects of the discontinuities at the endpoints of each segment.

# 3

## Materials and Methodology

### 3.1 Research Design

#### 3.1.1 Purpose

The primary purpose of this study is to investigate the impact of EMI on the performance of acoustic sensors used in electric aviation propulsion systems. Specifically, the research aims to evaluate how EMI influences the measurement accuracy and reliability of various vibro-acoustic sensors, including condenser microphones and triaxial accelerometers. By understanding these effects, the study seeks to provide insights into the sensor behavior under real-world conditions and identify potential challenges or limitations that may affect sensor performance in electrified aircraft propulsion systems. This knowledge is crucial for optimizing sensor design and ensuring accurate monitoring and control in future electric aviation technologies.

#### 3.1.2 Approach

The experiment was conducted at the [German Aerospace Centre \(DLR\) Institute of Flight Systems](#) in Braunschweig. By varying key parameters (explained in section [3.2.3](#)), the study aims to assess the impact of EMI on sensor performance. Data collected from these experiments are analyzed to evaluate changes in sensor readings and identify patterns or anomalies associated with EMI. In this study, immunity testing (Section [2.1.4](#)) of acoustic sensors against both conducted and radiated emissions by the electric motor has been investigated. For radiated and conducted immunity testing, the cables of all sensors

have been kept close to the power lines of the motor to induce EMI into the sensors. Also, accelerometers were placed on the motor to analyse the effect of conducted EMI. These tests, explained in Chapter 4, allowed us to comprehensively analyse the impact of EMI on sensor performance.

## 3.2 Materials & Equipment

### 3.2.1 Instruments Used

The experimental setup involved eight condenser microphones (section 2.2.1), selected based on their shielding characteristics and sensitivity. Four of these microphones were from the **GRAS 46BL** series<sup>[60]</sup> offering a frequency range from 4 Hz to 20 kHz, with dynamic range of 24 dB(A) to 146 dB and have a sensitivity of approximately 20 mV/Pa. The remaining four microphones were from the **Microtech Gefell M380** series<sup>[61]</sup>, which cover a frequency range of 20 Hz to 20 kHz, with dynamic range of 21 dB(A) to 135 dB and have a sensitivity of around 37.5 mV/Pa. The division into better shielded and less shielded types allowed for a comparative analysis of how shielding and sensitivity affect measurement accuracy. Two IEPE (Integrated Electronics Piezo-Electric) triaxial accelerometers (section 2.2.2) from **Kistler Type 8764B**<sup>[62]</sup> with a sensitivity of 100 mV/g<sup>1</sup> at 100 Hz were used. It has a center hole mounting permitting flexibility for 360° orientation.

For the experiment, the cables used in this experiment were sourced from Manufacturer **HUBER+SUHNER**. The cables of different shielding quality were used for different sensors to have a comparative study about how much EMI effect could be seen between the sensors with mitigation (section 2.1.5) and the ones without it. High-quality coaxial cable **RG188 A/U**<sup>[63]</sup> ( $d = 2.6$  mm,  $L = 5$  m), with a shielding effectiveness (see section 2.1.5) of 39 dB (upto 1 Ghz) and velocity factor<sup>2</sup> of  $v_f = 0.69$  was used for GRAS sensors. For Microtech Gefell microphones, the **RG174 U**<sup>[64]</sup> ( $d = 2.55$  mm,  $L = 10$  m), with shielding effectiveness of 40 dB (upto 1 Ghz) and  $v_f = 0.66$  was employed.

The DLR, Braunschweig had a custom-built radial-flux, permanent magnet synchronous motor (PMSM) with a maximum power rating of 5.67 kW and 8.5 Nm maximum torque

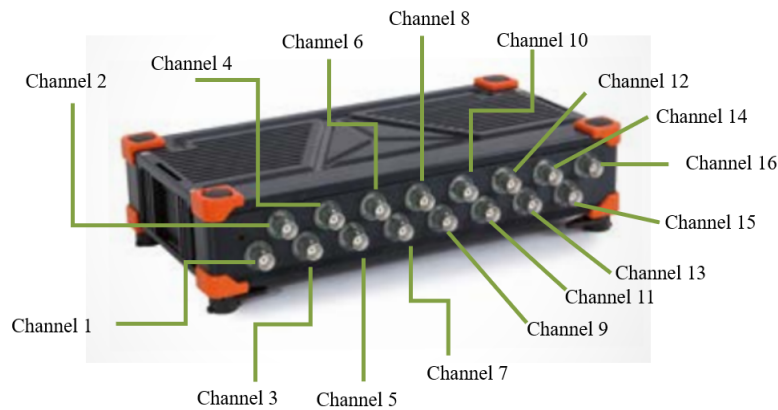
---

<sup>1</sup>1 g = 9.80 m/s<sup>2</sup>

<sup>2</sup>It describes the ratio of the speed at which an electrical signal propagates through a cable (or other transmission medium) compared to the speed of light in a vacuum.

driven by PWM inverter. The setup included a motor and a load mounted to it, which imitates the operation of a propeller on an electric engine. Additionally, a speaker was used to generate a reference audio signal.

DEWESoft data acquisition (DAQ) system, **SIRIUS<sup>®</sup> X** with 16 channels was used [65], as shown in Figure 3.1. The DEWESoft DAQ system provides a user-friendly interface that allows for real-time monitoring and analysis of the data collected from all sensors. The interface allows for easy setup and calibration, ensuring that all sensors are correctly configured before the start of the experiments.



**Figure 3.1:** DEWESoft DAQ System

The DAQ system is set to a high sampling rate of 100,000 Hz, which allows to accurately capture signals up to a specific frequency limit. This limit is determined by the *Nyquist theorem*, which states that to accurately sample and reconstruct a signal without aliasing<sup>3</sup>, the sampling rate must be at least twice the highest frequency present in the signal. This means that the DEWESoft DAQ system can accurately resolve and reconstruct signals with frequencies up to 50 kHz. Any signal component with a frequency higher than 50 kHz could lead to aliasing, where higher frequency signals are incorrectly interpreted as lower frequency signals due to insufficient sampling. By setting the sampling rate at 100 kHz, the DAQ system ensures that even rapid changes in the signal, which might occur at frequencies up to 50 kHz, are accurately recorded and analyzed.

The channel setup for the DEWESoft system is detailed in Table 3.1. Channel 1 is connected to the speaker via a signal generator. The signal generator produced a stepped

<sup>3</sup>Aliasing is the overlapping of frequency components resulting from a sample rate below the Nyquist rate.

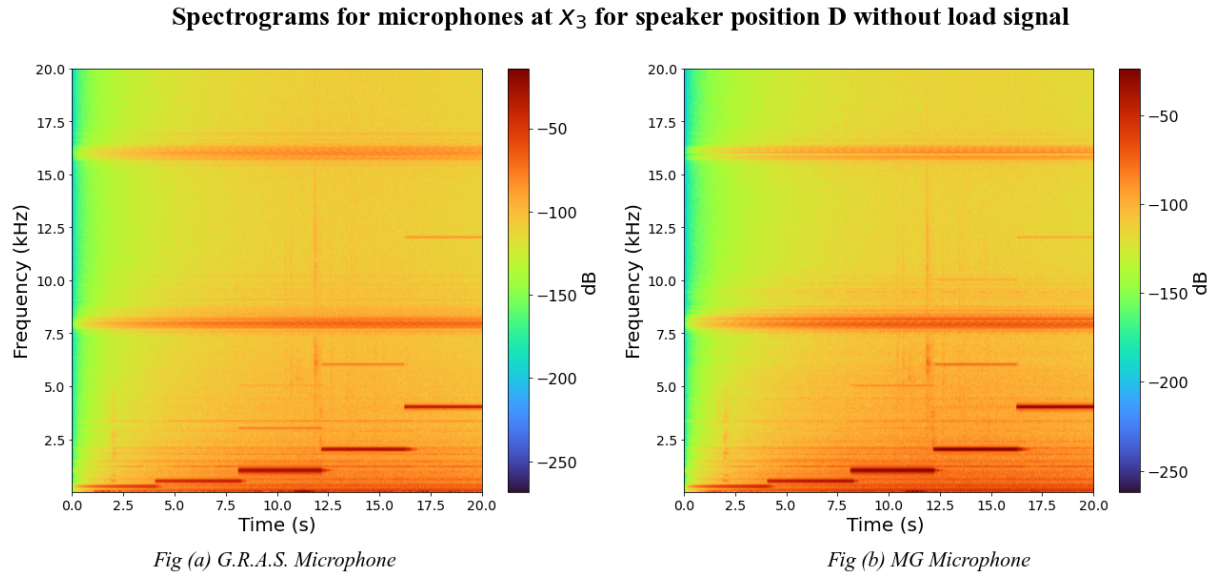
sine waves<sup>4</sup> at specific frequencies of 250 Hz, 500 Hz, 1000 Hz, ..., 16,000 Hz for a duration of 4 seconds each. By generating a stepped sine wave, the speaker is excited at various specific frequencies. This stepped approach is employed to systematically cover a broad frequency spectrum and identify specific frequencies that might be more susceptible to EMI. Channels 2 to 10 were allocated to the microphones, excluding Channel 6, captured data from the microphones in Pascals (Pa). Channels 11 to 13 recorded vibrational data from the accelerometers on the load in meters per second squared ( $\text{m/s}^2$ ), while Channels 14 to 16 captured vibrational data from the accelerometers on the motor.

Channel No.	Channel Name	Unit
AI 1	Speaker	V
AI 2	Gras 581878	Pa
AI 3	MG 275	Pa
AI 4	Gras 581525	Pa
AI 5	MG 277	Pa
AI 6	<i>Unused</i>	
AI 7	MG 285	Pa
AI 8	Gras 581511	Pa
AI 9	MG 283	Pa
AI 10	Gras 581516	Pa
AI 11	6299421 x	$\text{m/s}^2$
AI 12	6299421 y	$\text{m/s}^2$
AI 13	6299421 z	$\text{m/s}^2$
AI 14	6299419 x	$\text{m/s}^2$
AI 15	6299419 y	$\text{m/s}^2$
AI 16	6299419 z	$\text{m/s}^2$

**Table 3.1:** DEWESoft Channel Setup

Figure 3.2 display the frequency content of signals captured by G.R.A.S. and MG microphones  $x_3$  with speaker at position D. A spectrogram is a visual representation of the spectrum of frequencies in a signal as it varies over time. It displays time on one axis and frequency on another, with the intensity of each frequency at a given time shown using color or brightness. Notably, distinct horizontal lines (red regions) at specific frequencies around 2 kHz, 4 kHz, 8 kHz, 12 kHz, and 16 kHz are observed. These correspond to the frequencies generated by the signal generator.

<sup>4</sup>A sinusoidal signal whose frequency changes in discrete steps over time.



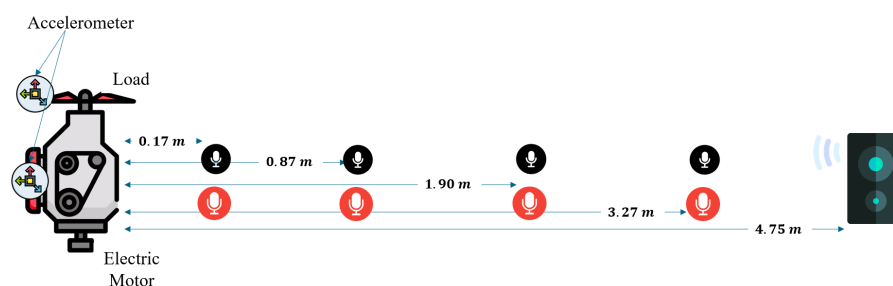
**Figure 3.2:** Spectrogram

### 3.2.2 Test Setup

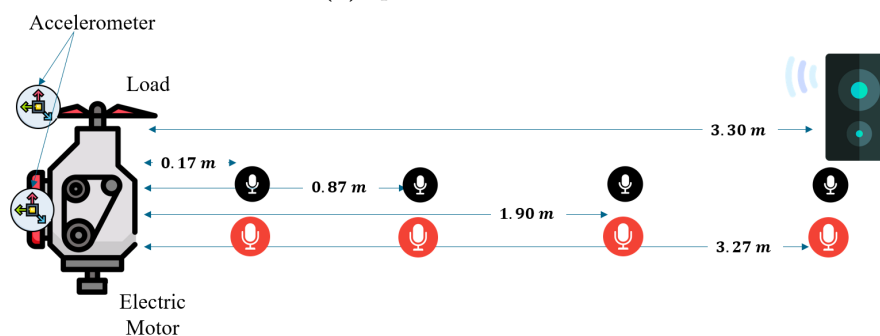
The microphones and accelerometers were strategically placed to ensure comprehensive data collection. According to Figure 3.3, four microphone positions were decided, each with a pair of microphones: one shielded and one regular. The microphones were positioned at specific distances from the electric motor:  $x_3$  at 0.17 meters,  $x_2$  at 0.87 meters,  $x_1$  at 1.90 meters, and  $x_0$  at 3.27 meters. These distances were chosen to capture the acoustic signals at various distances, enabling a thorough analysis of the EMI effects across different locations.

The accelerometers were attached directly to the electric motor and the load using adhesive materials to ensure firm attachment and accurate vibration measurement. One accelerometer was mounted on the electric motor to measure its vibrational characteristics, while the second accelerometer was mounted on the load to capture the vibrations transmitted to the load through the motor.

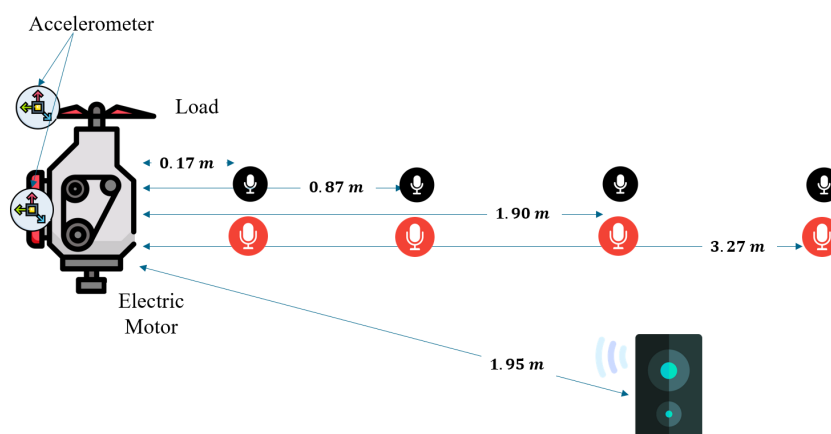
In addition to the sensor placements, the speaker was positioned at four distinct relative motor locations throughout the measurement area. The speaker positions are as follows: Position A at 4.75 m, Position B at 3.30 m, Position C at 1.95 m, and Position D at 0.93 m from the electric motor. These speaker positions were chosen to provide a consistent reference sound from different distances, facilitating a comprehensive evaluation of how EMI could affect acoustic measurements at various configurations.



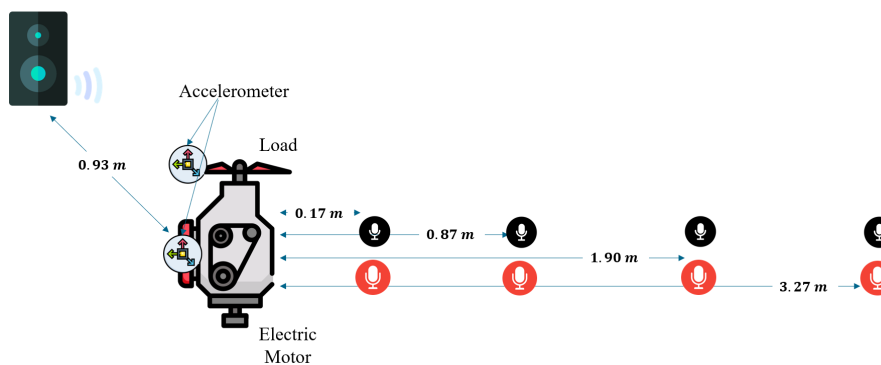
(a) speaker Position A



(b) speaker Position B



(c) speaker Position C

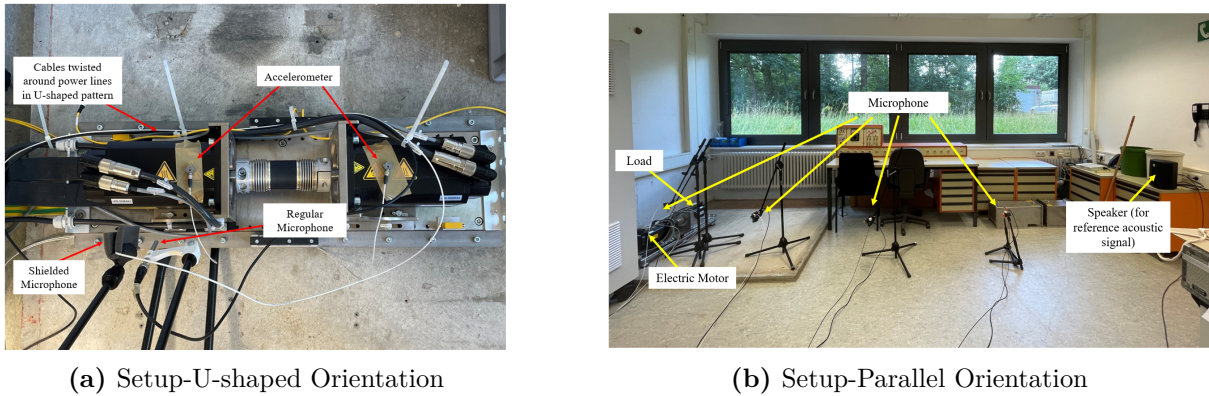


(d) speaker Position D

**Figure 3.3:** Measurement Setup with different speaker positions (black and red represent different types of microphones)



In the experimental setup, the orientation of the microphone cables relative to the power lines was a crucial variable. Different orientations can significantly influence the level of EMI experienced by the acoustic sensors, as explained in section 2.1.3. Initially, three distinct cable orientations were planned: parallel, perpendicular, and coiled in U-shaped pattern around the power lines (Figure 2.4). However, only two orientations were tested: parallel and U-shaped (Figure 3.4). These orientations were specifically selected to represent the extremes of cable positioning that might result in the highest and lowest levels of EMI.



**Figure 3.4:** Different types of cable orientations

### 3.2.3 Experimental Procedure

#### Calibration of sensors

Before any equipment was turned on, the microphones were calibrated using a **GRAS 42AG** calibrator<sup>[66]</sup>. This calibration process involved placing the calibrator over the microphones to generate a known sound pressure level, typically 114 dB at 1 kHz. The acceleration sensors were tested for functionality using the **Kistler Type 8501A**<sup>[67]</sup> mobile vibration calibrator.

#### Measurement Matrix

The measurements followed the systematic approach as outlined in Table 3.2. Initial sensor testing was conducted without the presence of EMI, i.e. when everything is turned off (background noise) to establish a baseline for comparison. After recording the background noise, only the motor signal at three different load conditions was recorded. The load conditions applied to the motor are enlisted in Table 3.3.

S.No.	Measurement type	Speaker Distance (m)	Motor load (W)
1	Background Noise	-	-
2	Only motor	-	$L_1$
3	Only motor	-	$L_2$
4	Only motor	-	$L_3$
5	Only speaker	A	-
6	speaker and motor	A	$L_1$
7	speaker and motor	A	$L_2$
8	speaker and motor	A	$L_3$
9	Only speaker	B	-
10	speaker and motor	B	$L_1$
11	speaker and motor	B	$L_2$
12	speaker and motor	B	$L_3$
13	Only speaker	C	-
14	speaker and motor	C	$L_1$
15	speaker and motor	C	$L_2$
16	speaker and motor	C	$L_3$
17	Only speaker	D	-
18	speaker and motor	D	$L_1$
19	speaker and motor	D	$L_2$
20	speaker and motor	D	$L_3$

Table 3.2: Measurement Matrix

Load Condition	RPM	Frequency (Hz)	Torque (Nm)	Power (W)
$L_1$	1125	18.75	14.00	1649.34
$L_2$	5700	95.00	7.90	4715.53
$L_3$	8000	133.33	4.83	4049.16

Table 3.3: Motor Specifications

Each measurement involved four different speaker positions (A, B, C, and D), with each position being tested under three load conditions ( $L_1$ ,  $L_2$ , and  $L_3$ ) and repeated for each cable orientation (parallel and coiled around the power lines). After background noise was recorded, measurements were initially conducted with only the motor turned on at the three different load conditions ( $L_1$ ,  $L_2$ , and  $L_3$ ). This was followed by measurements with only the speaker turned on to provide a reference audio signal. Finally, three additional measurements were performed with both the speaker and the motor turned on at the three different load conditions.

Setup data	
Microphone position (m)	
x <sub>0</sub>	3.27
x <sub>1</sub>	1.90
x <sub>2</sub>	0.87
x <sub>3</sub>	0.17
Accelerometer position	
a <sub>1</sub>	At motor
a <sub>2</sub>	At load
Speaker Distance (m)	
A	4.75
B	3.30
C	1.95
D	0.93

**Table 3.4:** Setup Data

This procedure ensured that a comprehensive set of data was collected to analyse the possible impact of EMI on the sensors as well as the speaker under various configurations and operational states. By systematically varying the load conditions and cable orientations, the study aimed to capture the full extent of EMI effects on the device under test, providing a robust dataset for subsequent analysis.

## 3.3 Data Analysis

### 3.3.1 Data Collection & Extraction

Time-signal data was collected from sensors using DEWESoft. The DAQ system recorded signals and stored the data in *.dxd* files. After data collection, the raw data was extracted in *.csv* format for ease of processing and analysis.

### 3.3.2 Signal Processing

After extracting the data, it was imported into Python using the **pandas** library, for further analysis. These signals are then preprocessed by removing their mean, which centers the signal around zero, and applying a *Hanning*<sup>5</sup> window to reduce spectral leakage during the Fourier Transform. After preprocessing, the signals are divided into

<sup>5</sup>The Hanning windowing function helps to smooth the signal, reducing the amplitude of discontinuities at the beginning and end of the data set.

smaller chunks, and an FFT is applied to each chunk to convert the signals from the time domain to the frequency domain. The resulting frequency-domain data is averaged across chunks to smooth the spectrum. The spectra are then converted into decibel (dB) scale (equation 2.21) using a reference pressure level to facilitate acoustic analysis.

Various FFT analysis techniques, as described in the section 2.3.1, were performed. These included magnitude spectrum analysis, power spectrum analysis and coherence analysis. These techniques provided a comprehensive understanding of the frequency-domain characteristics of the signals, crucial for addressing the research objectives.

Additionally, spectral subtraction analysis for the noisy signal was studied. According to equation 2.27, it can be expressed as:

$$|\hat{X}(f)|^2_j = |Y(f)|^2_{i,j} - \overline{|N(f)|^2}_i \quad (3.1)$$

where  $|\hat{X}(f)|^2$  is Estimated power spectrum for only speaker signals,  $|Y(f)|^2$  is Power spectrum for signals when both motor and speaker is ON and  $\overline{|N(f)|^2}$  is Averaged power spectrum for only motor signals.

In equation 3.1, index  $i$  refers to load conditions ( $L_1$ ,  $L_2$ , and  $L_3$ ) and index  $j$  indicates speaker positions ( $A$ ,  $B$ ,  $C$  and  $D$ ). The  $|\hat{X}(f)|^2$  obtained was plotted against the power spectrum of original recorded speaker signal  $|X(f)|^2$  to assess whether EMI had affected the speaker signal. This comparison provided insights into the extent of EMI's impact on the signal and its effect on signal clarity.

\*Please refer Appendix A for the algorithm used to compute spectral subtraction for power spectrum signals for this experiment.

# 4

## Results

In this chapter, we delve into the analysis of the experimental data collected during the study. The discussion that follows focuses on the general trends observed across all cases mentioned in Section 3, with particular emphasis on extreme case scenarios that might show some EMI effects. The extreme conditions considered for analysis are: microphones at  $x_3$ , with U-shaped cable orientation, speaker at D, and  $L_2$  load condition.

The analysis was conducted by comparing the sound pressure levels (SPL) in dB of the recorded microphone signals. This method allows for the identification and quantification of frequency components that may reveal the presence of EMI or other noise sources. The SPL is directly related to the amplitude of the sound waves generated by the mechanical vibrations in the system and can be expressed as:

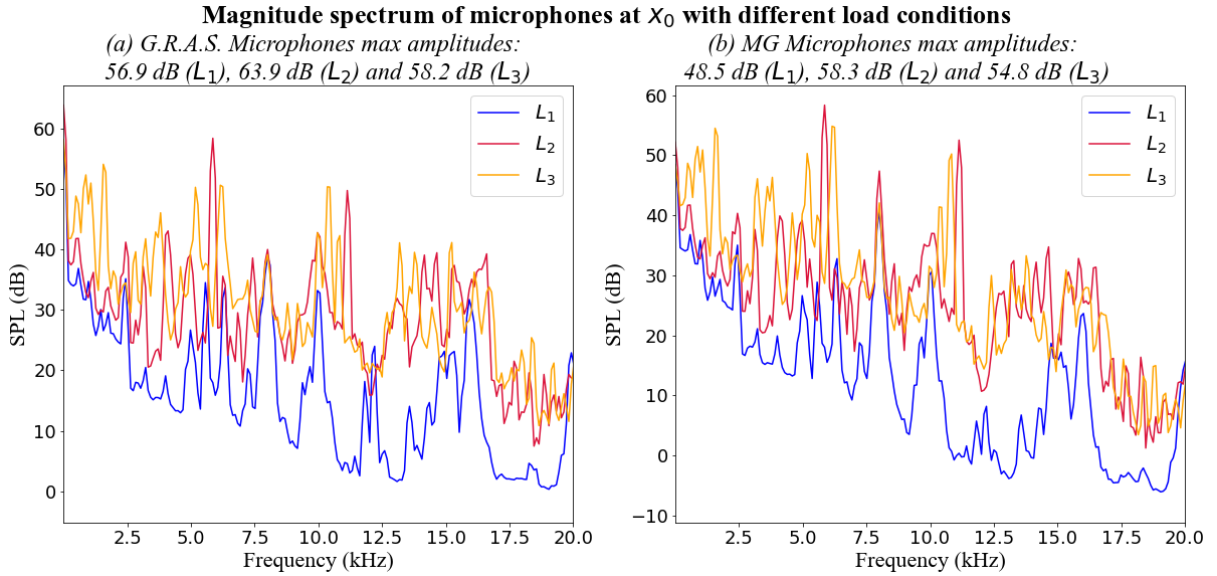
$$\text{SPL} = 20 \log_{10} \left( \frac{p}{p_0} \right) \text{dB} \quad (4.1)$$

where  $p$  is the sound pressure caused by the vibrations, and  $p_0$  is the reference sound pressure (20  $\mu\text{Pa}$  in air)<sup>[68]</sup>. For accelerometer, the magnitude spectrum is analysed in  $m/s^2$ .

### 4.1 Acoustic characteristics of the motor

For this analysis, the microphones farthest from the motor ( $x_0$ ) are chosen as the baseline measurement, because this positioning presumably minimizes the impact of EMI, providing a cleaner reference for analysis. This analysis is performed for only motor signals from the microphones with parallel configuration of cables in frequency range of 0-20 kHz,

as it corresponds to the audible frequency range. Changing the load conditions of the motor helps to see how different levels of stress on the motor affect the noise it produces. This variation can impact both the electromagnetic interference and the acoustic noise generated by the motor.



**Figure 4.1:** Magnitude Spectrum for microphones at  $x_0$  with different load conditions

Figure 4.1 depicts the SPL of the microphones at  $x_0$  during load condition  $L_1$ ,  $L_2$  and  $L_3$ . The magnitude spectra of G.R.A.S. and MG microphones under different load conditions reveal distinct behaviors across frequency ranges. In the lower frequency range (0-20 kHz), both microphone types exhibit the highest SPL values under load condition  $L_2$ , with G.R.A.S. microphones reaching a peak of 63.9 dB, which is higher than MG microphones peaking at 58.3 dB. This implies that the motor or system generates more noise as the load increases. The SPL under  $L_1$  remains consistently lower in both microphone types, while  $L_3$  follows a mid-range profile. In the higher frequency range (20-50 kHz), the SPL levels drop significantly across all loads, with none exceeding 30 dB. However,  $L_2$  still shows a comparatively higher response in both types of microphones.

The observed trend in the microphone data, where higher load conditions result in increased amplitudes and broader frequency content, can be primarily explained by the relationship between load and *Sound Pressure Level (SPL)* (equation 4.1). As the mechanical load increases, the motor experiences more intense vibrations, which transfer to the surrounding air, increasing the sound pressure  $p$ . This results in higher SPL values detected by the microphones. Higher loads also cause more complex vibrational behavior, leading to the generation of a broader range of frequencies. With greater vibrational

energy, more harmonics and resonant frequencies are excited, leading to the additional peaks observed at key frequencies.

The dominant frequency peaks are around 6 kHz, 8 kHz and 10-11 kHz for all load conditions, indicating tonal noise peaks and increased broadband noise at higher frequencies. The shift in dominant peak frequencies between  $L_2$  (11 kHz) and  $L_1$  (10 kHz) can be explained by the differences in the motor operating conditions, particularly RPM, torque, and power (Table 3.3). Under  $L_2$ , the motor runs at a much higher RPM (5700) compared to  $L_1$  (1125), leading to a higher excitation frequency (95 Hz vs. 18.75 Hz), which likely shifts the resonance to a higher frequency (11 kHz). Load condition  $L_3$  had the maximum RPM of 8000, but lowest Torque of 4.83 Nm, which causes the SPL levels to drop compared to load condition  $L_2$  with a torque of 7.9 Nm.

Having analyzed all load conditions, the subsequent sections will focus exclusively on higher load condition ( $L_2$ ) to further investigate the effects of increased motor load on the acoustic measurements. Although the frequency response range of the microphones is limited to 20 kHz, the analysis is extended to 50 kHz to detect potential EMI in higher frequency ranges.

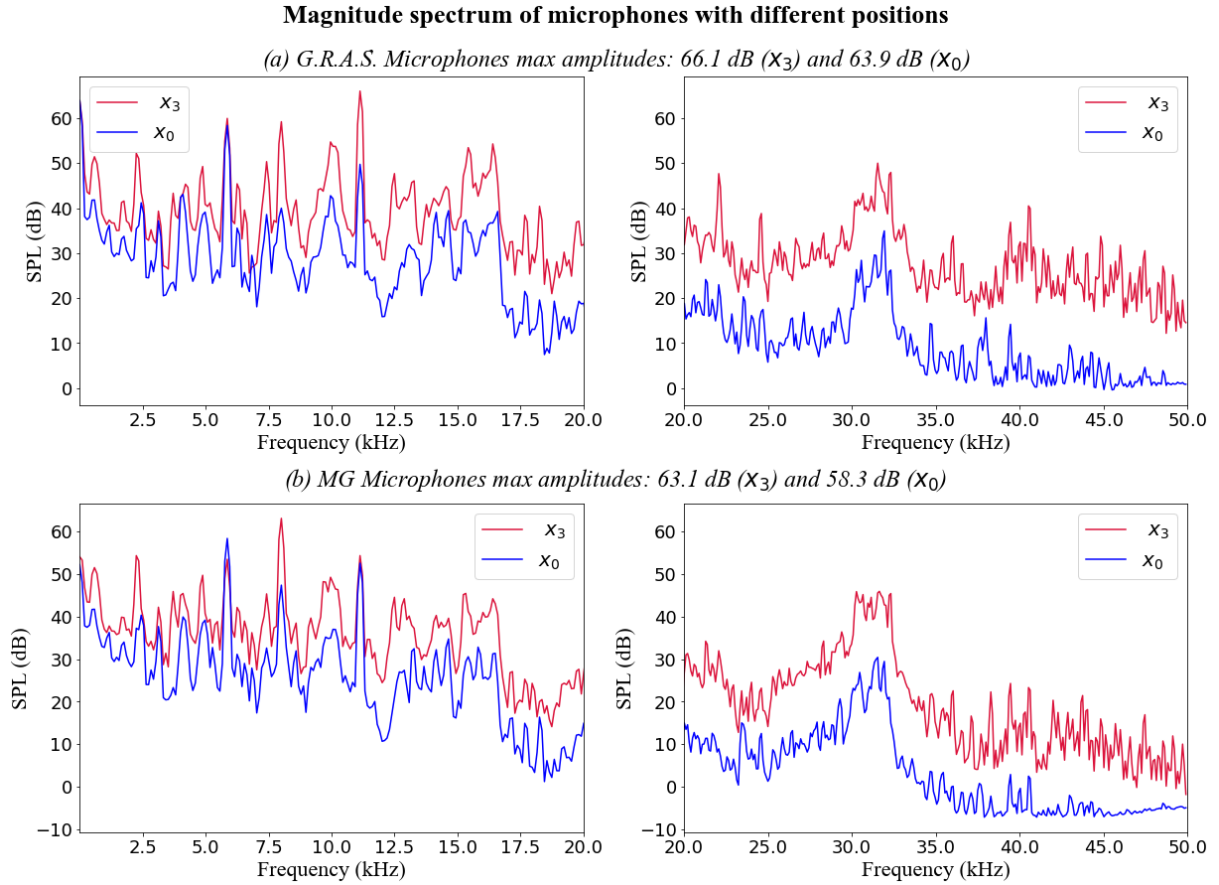
## 4.2 Effect of Microphone distance relative to motor

In figure 4.2, the magnitude spectra of microphones at  $x_3$  (closer to the motor) and  $x_0$  (farther from the motor) at load condition  $L_2$  and parallel configuration of cables are compared, based on reducing the microphone distance from the noise source. For this analysis, the speaker is turned OFF. Adjusting the microphone distance from the motor allows you to observe how noise levels change with proximity.

As expected, for the microphone positions ( $x_0$  and  $x_3$ ), the  $x_3$  position consistently shows higher amplitudes across all frequencies compared to  $x_0$ , particularly in the higher frequency range (above 20 kHz). This suggests that position  $x_3$  introduces more noise or interference for both the microphones, though the effect is more pronounced for the G.R.A.S. microphone. Peaks in the SPL are observed around 6 kHz, 8 kHz and 11 kHz for  $x_3$ , suggesting resonances in the system that are more pronounced at closer distances. The higher SPL at  $x_3$  (66.1 dB for G.R.A.S. and 63.1 dB for MG) compared to  $x_0$  (63.9 dB and 58.3 dB, respectively) indicates that closer proximity leads to better detection of high-frequency content and resonant behavior in the system. No additional peaks or unusual noise characteristics were observed in either microphone, which could be



attributed to EMI, indicating that both responded similarly to the overall acoustic and mechanical noise, with the closer position  $x_3$  capturing more intense and detailed noise components compared to the farther position ( $x_0$ ).



**Figure 4.2:** Magnitude Spectrum for microphones with different locations relative to the motor

The trends observed in the magnitude spectra for the variation of microphone distance relative to the motor can be explained by *inverse square law* of sound propagation<sup>[69]</sup>. According to this law, sound pressure decreases proportionally to the square of the distance from the source. Mathematically, this is expressed in equation 4.2:

$$SPL(r) = SPL_0 - 20 \log_{10} \left( \frac{r}{r_0} \right), \quad (4.2)$$

where  $SPL(r)$  is the sound pressure level at a distance  $r$ ,  $SPL_0$  is the reference sound pressure level at a distance  $r_0$  and  $r$  is the distance from the sound source.

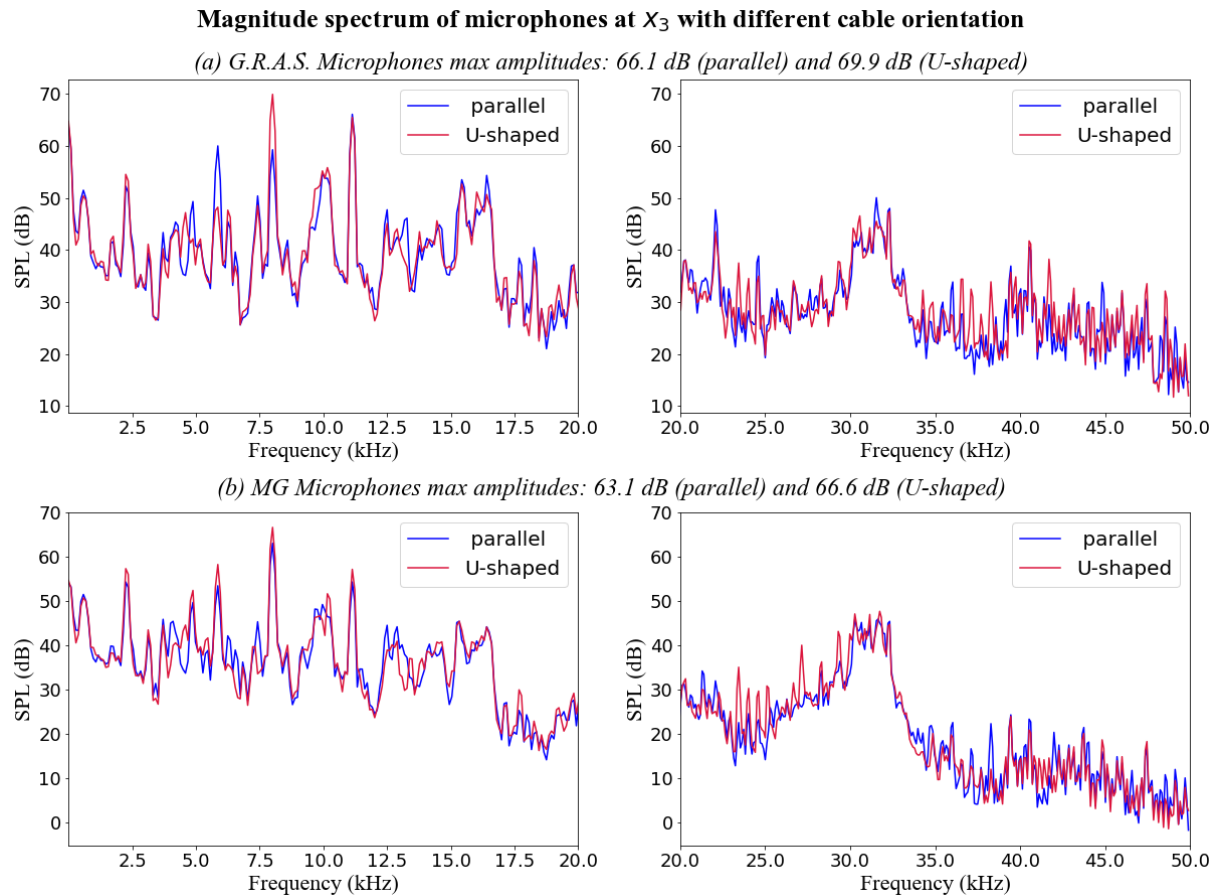
Microphones positioned closer to the motor ( $x_3$ ) exhibit higher amplitudes due to their proximity to the mechanical noise and sound sources. The closer the microphones are to



these sound sources, the higher the acoustic pressure, resulting in increased signal amplitudes. In this case, the distance between the source and the microphones changes, with shorter distances leading to higher recorded noise levels.

After exploring all microphone positions, the following sections will focus solely on the closest microphones to examine their responses in detail, as no significant effects were observed in the furthest microphones.

### 4.3 Contribution of cable orientation



**Figure 4.3:** Magnitude Spectrum for microphones with different cable orientations

As discussed in section 2.1.3, most EMI occurs in cable which prompted the study with different cable orientations. Figure 4.3 compares the magnitude spectrum of signals recorded by both the G.R.A.S. and MG microphones closest to the motor ( $x_3$ ) for two different cable orientations (section 3.2.2) at load condition  $L_2$  with speaker turned OFF.

The magnitude spectra of microphones at position  $x_3$ , comparing parallel and U-shaped cable orientations, show that both the configurations follow similar pattern overall. In the G.R.A.S. microphones, the maximum SPLs are 66.1 dB (parallel) and 69.9 dB (U-shaped), with noticeable differences around 8 kHz and 11 kHz, where the U-shaped orientation produces higher values. Similarly, the MG microphones exhibit maximum SPLs of 63.1 dB (parallel) and 66.6 dB (U-shaped), with the U-shaped configuration again showing elevated levels at key frequencies such as 8 kHz. The U-shaped cable orientation might exhibit higher peaks at certain frequencies due to the influence of mechanical noise caused by the motor. Since the cables were directly coiled around the motor, they were more susceptible to vibrations generated by the motor's mechanical components, particularly at higher frequencies.

Alternatively the increased noise might be due to EMI because this configuration of cables is more susceptible to EMI and can act like antenna (section 2.1.3). Possible EMI frequencies can be estimated by considering the cable length. Using the velocity factor  $v_f$  for both cables (see section 3.2.1), we calculated the frequencies at which the cables may act as antennas based on the quarter-wavelength resonance formula<sup>[70]</sup>:

$$f = \frac{v_f \cdot c}{4L} \quad (4.3)$$

where  $c = 3 \times 10^8$  m/s is speed of light and  $L$  is the cable length. For the G.R.A.S. microphone, the resonant frequency is 10.35 MHz, and for the MG microphone, the resonant frequency is 4.95 MHz (see section 3.2.1 for cables specifications). These frequencies are far higher than the 50 kHz range observed in the plots, which means the cables would not act as antennas at the frequencies of interest in this experiment. Therefore, the peaks observed are more likely due to mechanical noise and vibrations rather than radiated EMI from the cables acting as antennas.

However, higher order harmonics of these frequencies can fold back into the first Nquist zone<sup>1</sup> due to aliasing<sup>[71]</sup>. Hence, it is important to check aliased frequency ( $f_a$ ) for both the microphones. Equation 4.4 explains the calculation of aliased frequency.

$$f_s = |\text{closest integer multiple of } f_s \times f_s - f| < f_N \quad (4.4)$$

where  $f_s$  is the sampling frequency,  $f$  is the signal frequency (here, resonant frequency of microphones) and  $f_N = f/2$ .

For G.R.A.S. microphone, the closest multiple of  $f_s$  is round  $f/f_s = 103.5 \approx 104$ . So,

---

<sup>1</sup>Frequencies between 0 and  $f_N$  (the Nyquist frequency).

$f_a = |0.1n \times 10^6 - 10.35 \times 10^6| < 50 \times 10^3$  Hz. For  $n = 104$ ,  $f_a = 50$  kHz.

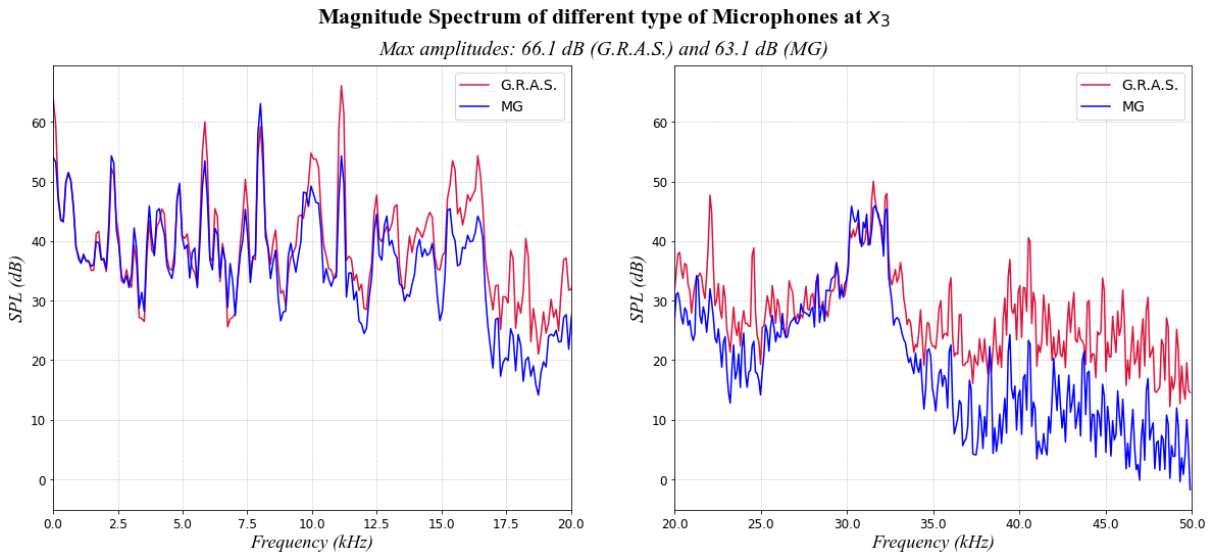
Similarly, for MG microphone, the closest multiple of  $f_s$  is round  $f/f_s = 49.5 \approx 50$ . So,  $f_a = |0.1n \times 10^6 - 4.95 \times 10^6| = < 50 \times 10^3$  Hz. For  $n = 50$ ,  $f_a = 50$  kHz.

Hence, no aliasing effect will be seen within the range 0-49.99 kHz. At 50 kHz, both aliased signals will appear. This might cause borderline effect, but no aliasing will occur below 50 kHz.

The U-shaped cable orientation was utilized only for the closest microphones without speaker signals. To ensure a continuous flow in the investigation, the parallel cable configuration was chosen for studying signals with both speaker and motor signals.

## 4.4 Role of Microphone type

Examining different microphone types is important because each has varying sensitivities and noise rejection capabilities, which can affect how accurately motor noise and EMI are measured. The magnitude spectrum of signals from different type of microphones at  $x_3$  are analysed in figure 4.4 with parallel configuration of cables at load condition  $L_2$  and no speaker signal.



**Figure 4.4:** Magnitude Spectrum of different type of microphones at  $x_3$

The G.R.A.S. microphone consistently exhibits higher sound pressure levels (SPL) than the MG microphone across the frequency range. The G.R.A.S. microphone reaches a maximum SPL of 66.1 dB, compared to 63.1 dB for the MG microphone. In the 0–20 kHz

range, G.R.A.S. microphone demonstrates more prominent peaks, particularly around 6 kHz, 8 kHz, 11 kHz, and 16 kHz, while both microphones follow similar general trends with tonal peaks. In the 20–50 kHz range, the differences become more pronounced, with broadband noise .

The higher SPL peaks observed with the G.R.A.S. microphone compared to the MG microphone could be attributed to several factors. Cable grounding and environmental factors, such as proximity to noise sources, room reflections or microphone directivity<sup>2</sup> may amplify these differences. Additionally, differences in diaphragm design, build quality, and material might also contribute. It is also important to consider that certain peaks might arise from unexplained behavior of microphones or experimental inaccuracies. For instance, foam around the microphone (figure 3.4a) could be blocking or attenuating certain signals, affecting the overall measurement. Moreover, the placement difference of microphones for higher frequencies (see figure 3.4a) might cause an evident difference, as the placement distance represents a large phaseshift for small wavelengths. Furthermore, noise from the motor at specific angles of directivity could contribute to variability in the recorded SPL peaks. Therefore, a comprehensive evaluation of these aspects is essential to accurately interpret the differences in SPL measurements between the microphones.

Given that the G.R.A.S. microphones exhibited unusually higher SPL in the previous sections, but no evident effect of EMI, the signals from these microphones were compared with both speaker and motor noise.

## 4.5 Influence of Speaker position

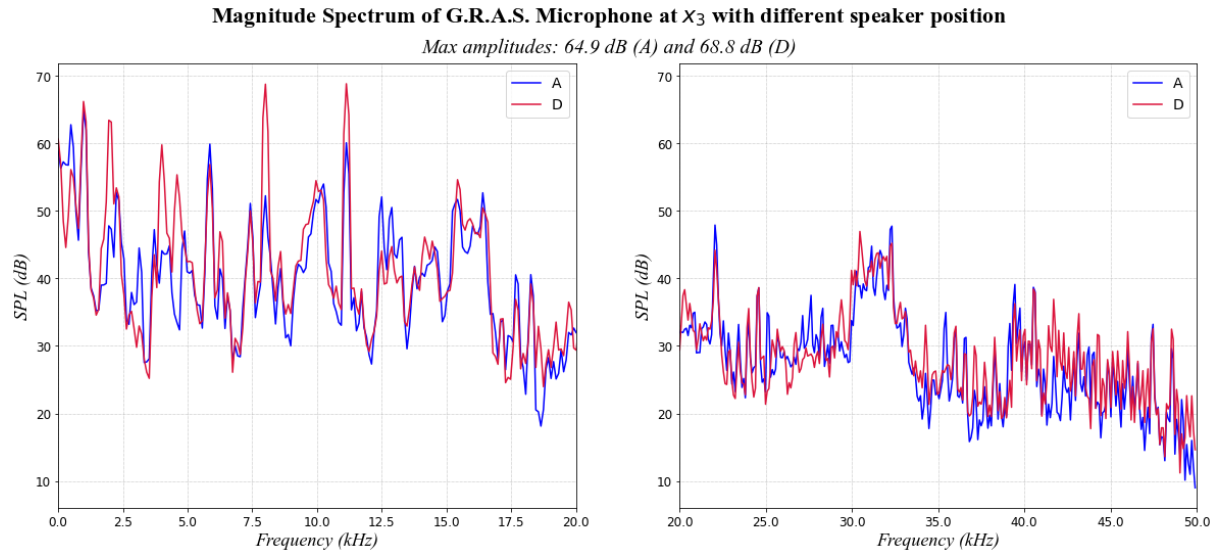
For this analysis, the speaker was turned ON alongside the motor to assess how the motor’s noise interferes with the speaker’s sound. Figure 4.5 explains the magnitude spectrum trend between signals from the G.R.A.S. microphones nearest to motor ( $x_3$ ), while changing speaker positions relative to the motor (A to D). Both the analysis are conducted on higher load condition  $L_2$  and all the microphones have parallel cable orientation.

Position D, consistently produces higher sound pressure levels (SPL) than position A across the spectrum. The maximum SPL for position D is 68.8 dB, compared to 64.9 dB for position A. The noise peaks observed while speaker is at position D are more pronounced when speaker is at position A. For higher frequency range (20-50 kHz), both

---

<sup>2</sup>Microphone directivity refers to the sensitivity of a microphone to sound coming from different directions, determining how well it captures or rejects sound based on its angle of incidence.

signals have almost identical spectra of broadband characteristic.

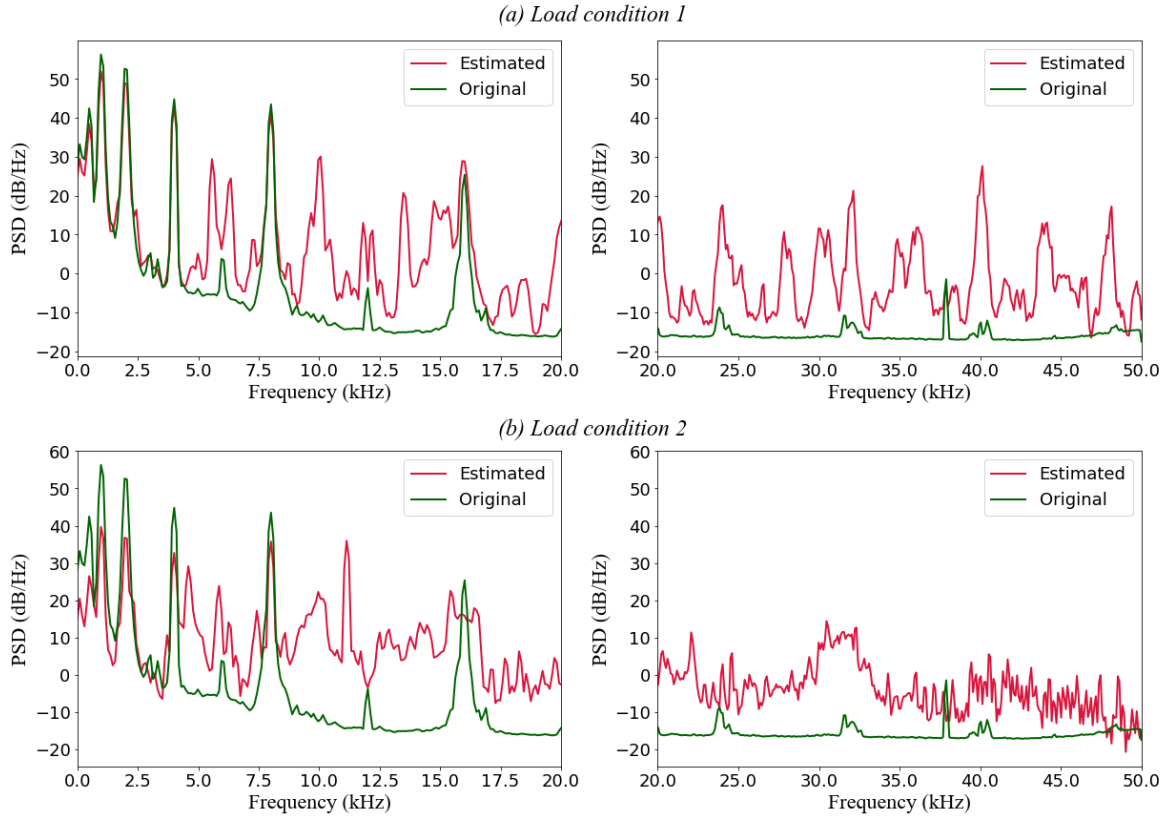


**Figure 4.5:** Magnitude Spectrum for microphones with different speaker positions relative to the motor

As already explained in section 4.2, the closer the noise source is, the higher the SPL (equation 4.2). Therefore, position D, being closer to the motor, should induce maximum noise or EMI into the speaker due to small distance from motor. Hence, the microphone results in higher SPL values due to shortest the distance between microphone and speaker. However, the comparison of the spectra reveals negligible EMI impact.

To further assess the potential impact of electromagnetic field on the speaker, spectral subtraction was used (see section 3.3.2). This technique involves subtracting the motor noise spectrum, recorded with no speaker excitation, from the motor noise spectrum when the speaker is active. Specifically, we subtract the power spectrum of the motor-only signal from the power spectrum of the motor-plus-speaker signal to obtain an estimated power spectrum of speaker-only signal.

Figure 4.6 illustrates the spectral subtraction process analysis across different load conditions for the G.R.A.S. microphones at  $x_3$ . The plots reveal that at low frequencies and particularly under load condition  $L_1$  (low RPM), the spectral subtraction method isolates the speaker signal from the motor noise. All speaker signal peaks are visible. Notably, small peaks observed in the original signal correspond to the first harmonics of our excitation frequencies.

**Spectral Subtraction of G.R.A.S. Microphone at  $X_3$  with speaker position D at Different Load Conditions**


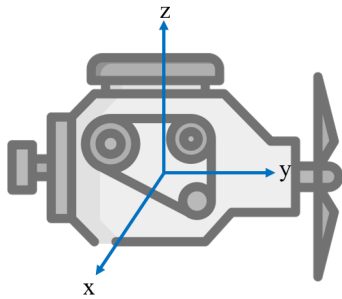
**Figure 4.6:** Spectral subtraction of microphones closest to the motor

However, as the speaker frequency or the load conditions increase, spectral subtraction becomes less accurate. Additional peaks appear in the spectra of the estimated power compared to the original signal. Acoustic analysis of the motor (section 4.1), along with the assumptions in the spectral subtraction method namely, the assumption of constant motor noise characteristics and accurate alignment of the subtraction process, suggest that these additional peaks are likely due to errors in the spectral subtraction rather than EMI.

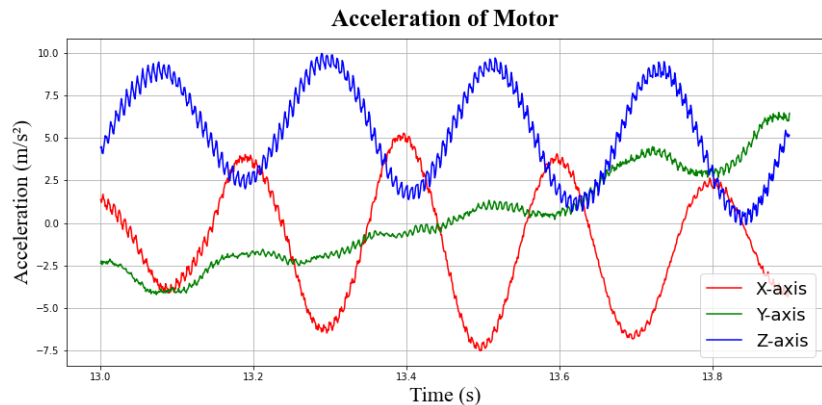
Furthermore, the strong directivity of the speaker at high frequencies may contribute to these errors. The microphones might not have captured sufficient energy from the speaker at these high frequencies, resulting in lower amplitude speaker signals compared to the motor noise. Consequently, while not entirely definitive, this analysis suggests that EMI is unlikely to be present in the speaker signal.

## 4.6 Acceleration Sensors

Since no EMI is found in the microphones, a correlation between the data recorded by the microphones and the accelerometers can be used to evaluate the acceleration sensors regarding possible EMI. According to theory Structural vibrations of the motor represent the dominant tonal noise. Thus, in case a low correlation between dominant noise events and spectrum of acceleration is observed, the acceleration sensor might be under EMI. By comparing the noise spectrum captured by the microphones with the vibrational data recorded by the accelerometers, it is possible to determine which components of the noise are attributed to mechanical sources and which are the result of airborne noise or EMI. This approach provides a more detailed characterization of the motor's noise behavior, allowing for the identification and separation of vibration-induced noise from acoustic emissions, thereby enhancing the understanding of the motor's operational noise profile. Figure 4.7 illustrates the acceleration axes of accelerometers, with the z-axis perpendicular to the motor. The x and y axes lie in the horizontal plane relative to the motor, with the x-axis directed towards the microphone setup.



**Figure 4.7:** Directions of axis relative to motor



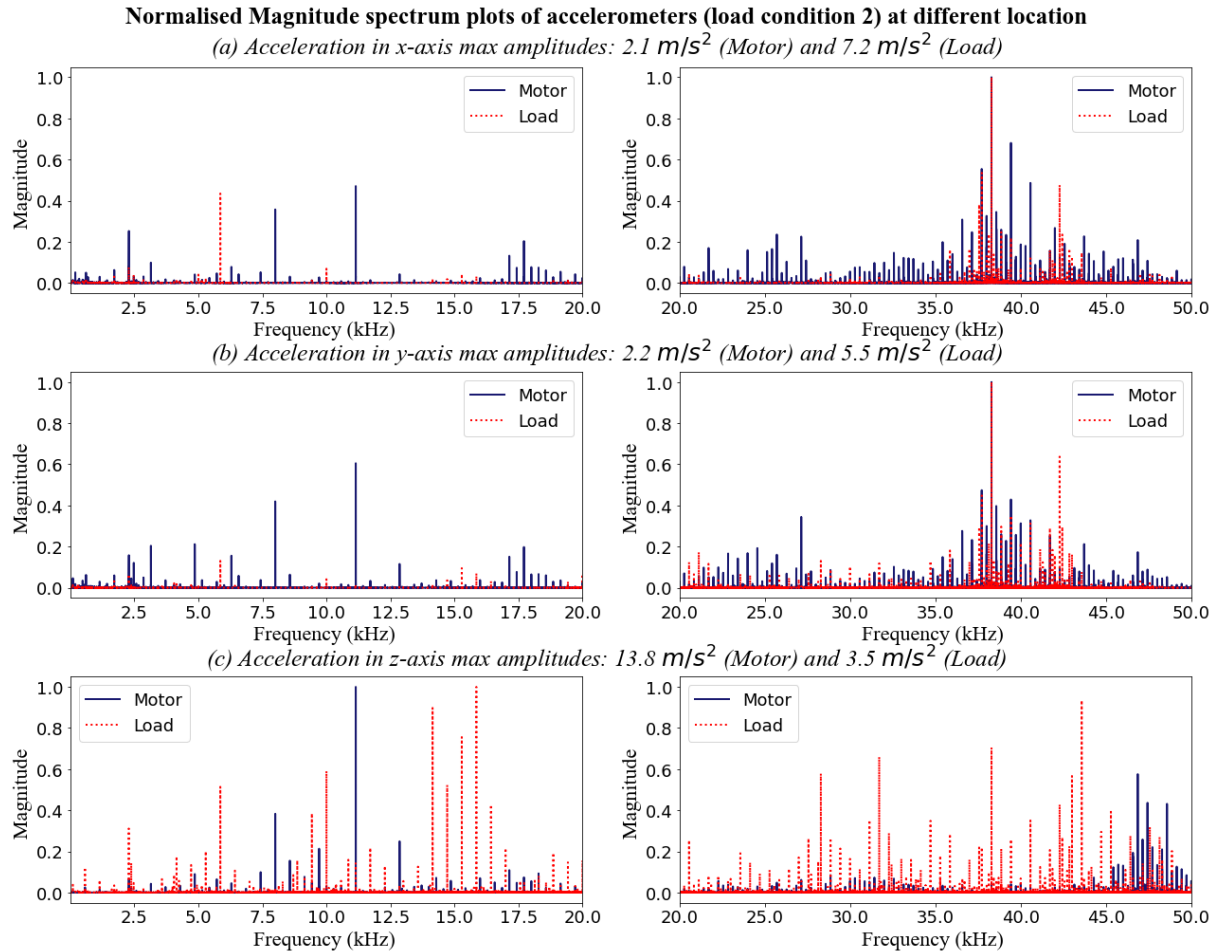
**Figure 4.8:** Acceleration of motor in time-domain

As discussed in section 2.2.2, the high-frequency distortions due to EMI might appear as sharp spikes or dropouts in time-domain signal of vibration. Therefore, figure 4.8 illustrates the analysis conducted to investigate this phenomena. The plot shows only a 10-second segment of the recording to highlight any distinct peaks or anomalies that may occur over milliseconds. Despite this focused view, the analysis across the full signal length reveals that all axes display clear periodic behavior with consistent peaks, indicating stable oscillatory motion over time. The signals are sinusoidal, with consistent amplitude and frequency, suggesting smooth and regular operation of the underlying system. Overall, no significant disturbances or anomalies are apparent in the peaks, reinforcing the observation



of regular, periodic motion. The time data analysis indicates no EMI effects.

In figure 4.9, the magnitude spectrum of accelerometers at load and motor, normalized to their respective maximum amplitudes, is compared in all three axis with load condition  $L_2$ . The plot shows that much more significant vibrations are found on the motor for all axes, but the larger amplitudes for x and y are found for the load, with maximum amplitudes of  $7.2 \text{ m/s}^2$  (x-axis) and  $5.5 \text{ m/s}^2$  (y-axis). In contrast, the motor shows smaller peaks of  $2.1 \text{ m/s}^2$  (x-axis) and  $2.1 \text{ m/s}^2$  (y-axis), suggesting less intense vibrations in these axes. However, in the z-axis, the motor dominates with significantly higher vibrations, peaking at  $13.8 \text{ m/s}^2$  and displaying strong activity in the 10-15 kHz range, whereas the load is much weaker, with a maximum amplitude of  $3.5 \text{ m/s}^2$ . This indicates that the load is more affected by vibrations in the x and y axes, while the motor experiences substantial vibrations along the z-axis at higher frequencies.

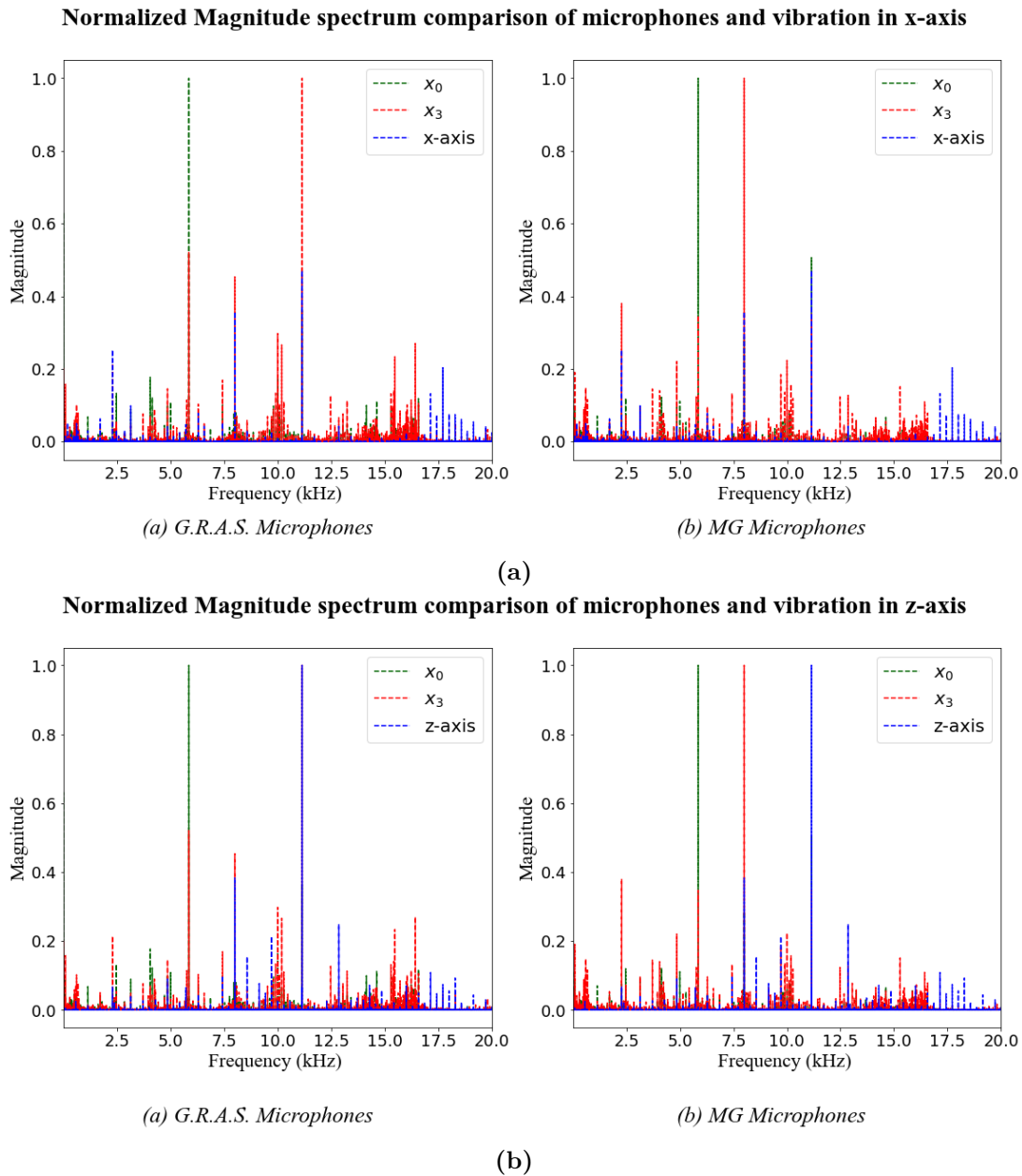


**Figure 4.9:** Normalized Magnitude spectrum of accelerometers at different location

The frequency range of accelerometers is 15 kHz, therefore the behavior above this range



is undefined by manufacturer. Moreover, in higher frequency range (above 30 kHz), motor experiences high peaks in all the axes, particularly x and z-axis. Looking back at the plots in section 4.1-4.5, there is sudden increase of SPL in the frequency range 30-35 kHz. The vibrations caused by the motor in x and z-direction might influence this increase in magnitude. Therefore, considering those peaks as an effect of EMI would not be necessarily true.

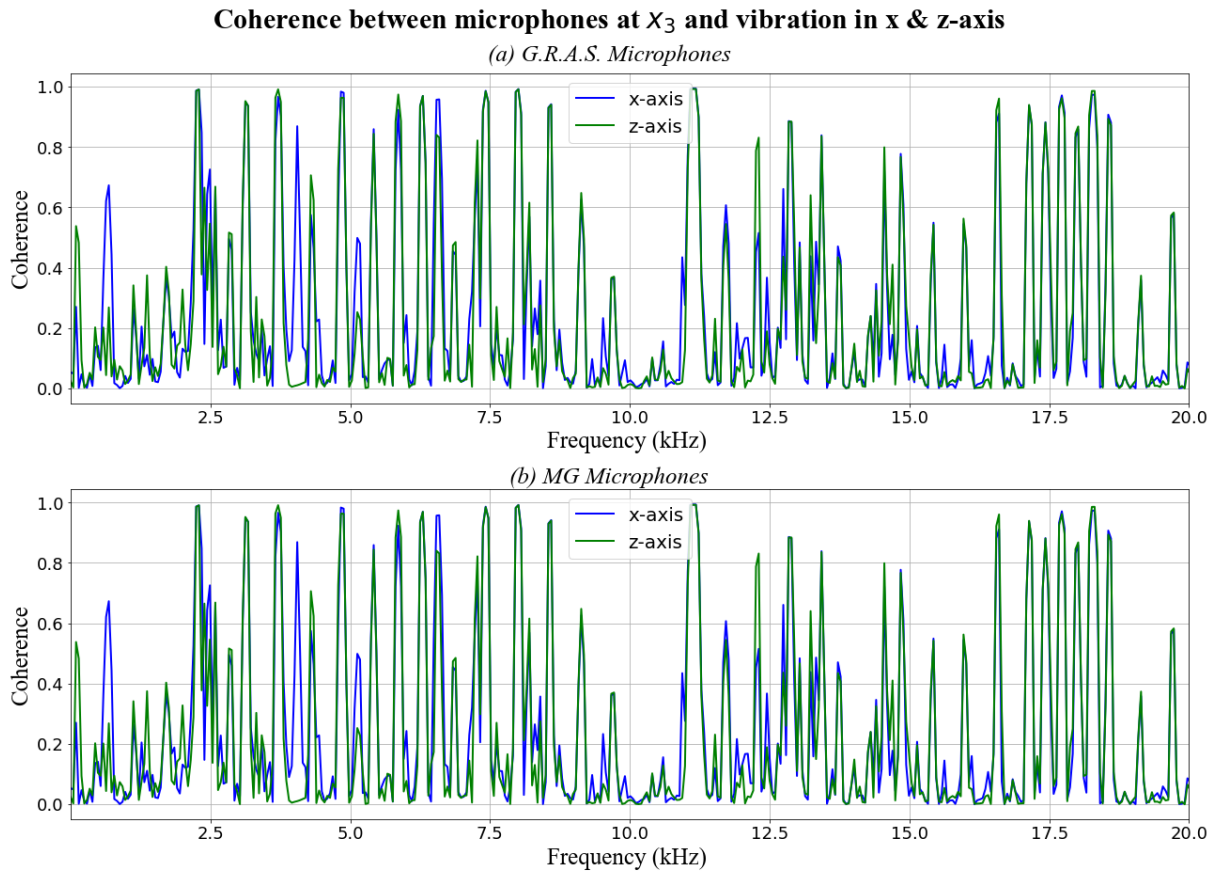


**Figure 4.10:** Normalized Magnitude spectrum comparison of microphones at  $x_3$  and vibration in x & z-axis

Figure 4.10 presents a detailed comparative analysis of the microphone signals alongside

the vibrations detected along both the x and z-axis with load condition  $L_2$ . These axes were selected because the x-axis aligns with the direction of the microphone setup, directly influencing the acoustic signals. The z-axis, being perpendicular to the motor, captures the primary vertical vibrations essential for understanding the motor's mechanical activity. The y-axis was not chosen as it lies perpendicular to the main direction of interest and does not significantly contribute to the correlation between motor vibrations and the acoustic signals recorded by the microphones.

According to figure 4.9, it is quite evident that the motor has a peak acceleration in all axes at 8 kHz and 11 kHz. Hence, causing vibrations in surrounding air in y-axis which leads microphones at  $x_3$  to capture a peak at 8 kHz. The strongest correlation between the microphones and y-axis vibration is around 11 kHz for the G.R.A.S. microphone and at 8 kHz for the MG microphone, where both the accelerometer and microphones show high magnitude peaks. This suggests that the motor's y-axis vibrations are effectively coupling with the air, producing acoustic waves at these frequencies. Additionally, the motor's vibrations along the z-axis at 8 kHz and 11 kHz with higher magnitude than x & y-axis (section 4.6) were transmitted through the ground, causing the microphones to pick up these vibrations. In the z-axis comparison plot (figure 4.10b), both G.R.A.S. and MG microphones again show peaks at key frequencies, particularly at 11 kHz, which closely aligns with the microphone data.



**Figure 4.11:** Coherence of microphone signals at  $x_3$  and vibrations in x & z-axis

The coherence plots (figure 4.11) for both G.R.A.S. and MG microphones in y & z-axis show a strong correlation between microphone signals and vibration at specific frequency bands, particularly in the ranges of 2–8 kHz, 11–13 kHz, and 17–19 kHz, with both microphones exhibiting peaks in coherence. Both types show a similar overall pattern and maximum coherence occurs around 11 kHz, which can be agreed based on the magnitude spectrum peak of accelerometers and microphones. This consistency in coherence across both microphones supports the argument that the significant frequency information captured by the microphones is of acoustic nature, specifically noise emitted by the motor, rather than being due to EMI. The coherence plots effectively reinforce this argument and complement the observations made in the figure 4.10.

## 4.7 Discussion of the results

The findings of this study suggest that EMI had minimal impact on the performance of the acoustic sensors used in this experiment. Instead, the primary factor influencing the

sensor readings was mechanical vibrations from the motor. These vibrations produced tonal noise at distinct frequencies in the spectrum, as illustrated in figure 4.10 by peaks observed in both G.R.A.S. and MG microphones, particularly along the z-axis.

The variations in load conditions highlighted that increased mechanical load led to stronger vibrations, which were detected by the sensors as additional noise in the frequency spectrum. This reinforces the conclusion that mechanical vibrations, rather than EMI, were the dominant source of interference in the acoustic measurements. Coherence analysis between microphone signals and motor vibrations further confirmed a close relationship, with higher coherence observed in frequency ranges corresponding to the motor's operational characteristics.

Additionally, the motor vibrations caused the cables to move, thereby inducing extra mechanical noise into the data. The comparison of different cable orientations revealed that the U-shaped configuration, which is more susceptible to cable movement, exhibited higher noise levels. This suggests that the mechanical vibrations from the motor contributed to additional noise in the cables, mainly at the dominant structural resonance, which can mimic EMI effects but is actually a result of the mechanical interference. The parallel cable orientation, less affected by such movements, showed reduced noise levels, further supporting the idea that EMI did not significantly alter the acoustic measurements.

Reducing microphone distance from the motor resulted in higher SPL, but there were no additional peaks observed in the spectrum of closest microphones. Similarly, varying the speaker distance also provided results that agree theoretical definitions. The closest position of speaker resulted in higher amplitudes. This is expected, as the proximity of microphone from the sound source is shortest.

Use of different type of microphones resulted in similar behavior for lower frequency range. However, at higher frequency the microphones had a difference of  $\approx 10$  dB. This might be because of several factors such as sensitivity, shielding factor, environmental factors and so on. Anyhow, the spectra followed a similar pattern at higher frequencies despite the difference in absolute level.

The correlation between the signals from microphones and accelerometers further suggest that the unexplained peaks observed in the spectra of microphones were due to the vibrations caused by the motor in x & z-axis.

In summary, the results indicate that EMI was not a major contributor to the observed sensor responses. It had almost negligible presence. Instead, mechanical noise from the motor and its vibrations played a significantly more prominent role in influencing the sensor signals.

## 4.8 Limitations

### Accelerometer Placement Limitation

The accelerometers were attached to the motor using duct tape because initially using mounting wax proved ineffective; the heat generated by the motor caused the wax to soften and the sensors to detach. Although duct tape provided a temporary solution, it may not have ensured the most secure attachment, potentially leading to slight movements or detachment of the sensors during data collection. Screwing the sensors into the motor was not a feasible option during the experiment. To enhance the reliability of vibration measurements in future studies, alternative methods should be explored, such as using high-temperature adhesives or custom mounting brackets, to ensure stable sensor positioning and accurate data collection.

### Motor Power Limitation

The motor used in this study had a power rating of 5 kW, which is significantly lower than the power levels of motors typically used in electric aviation systems (Project [LU\(FT\)<sup>2</sup>](#)). As a result, the EMI generated by this motor may not fully reflect the intensity of EMI that would be produced by higher-powered motors in real-world aviation applications. This limitation could lead to an underestimation of EMI effects in environments where larger motors are used. Future research should aim to replicate these experiments with more powerful motors to provide a better understanding of the true EMI impacts on acoustic sensors.

### Uncontrolled Environment

The experiments were conducted in an uncontrolled environment, which may have introduced uncontrolled variables such as ambient noise, environmental noise and acoustic room reflections. These factors could influence the accuracy of the measurements. Conducted and radiated EMI could not be quantified. Performing the experiments in a controlled environment, such as an anechoic or reverberation chamber, would eliminate these external factors and provide more reliable data.

# 5

## Conclusion and Outlook

### 5.1 Conclusion

This study investigated the effects of electromagnetic interference (EMI) on the performance of acoustic sensors used in electric aviation propulsion systems, specifically examining the influence of a 5 kW motor. The results showed that electromagnetic interference had no visible impact on the sensor readings under the given conditions. This suggests that electromagnetic interference may not be a critical concern for lower-power motors in electric propulsion systems. Although various sensor configurations, shielding techniques, and cable orientations were tested, the interference levels remained low, and no significant degradation in sensor performance was observed.

The data analysis showed that different cable orientations, such as U-shaped versus parallel alignment relative to the power lines, did not cause any evident effect to the sensors. Proximity of sensors and speaker to the electric motor was another variable considered, with sensors placed at various distances. As expected, sensors closer to the motor experienced higher levels of noise but no exceptional behavior was observed in the spectra of signals which could be linked with electromagnetic interference.

The study also examined the impact of varying load conditions on the motor. Higher loads were associated with slightly increased noise sound pressure levels, particularly in the microphones closer to the motor. Nevertheless, nothing conclusive related to distortions caused by electromagnetic interference.

Additionally, acoustic signals captured by microphones were correlated to the vibrations recorded by accelerometers, which suggested that the additional peaks observed in micro-

phone signals was nothing else but the mechanical noise and vibrations by the motor.

The primary objective was to speculate some distortions related to electromagnetic interference in acoustic measurements. However, the study highlighted the dominant role of mechanical noise and vibrations, which were found to have a more significant effect on the accuracy of the sensor data.

## 5.2 Outlook

Looking ahead, further research is needed to explore the effects of electromagnetic interference in environments with higher-powered motors, such as those commonly used in commercial electric aviation, which range from 50 kW to 100 kW. These motors are likely to generate stronger electromagnetic fields, potentially amplifying the effects of electromagnetic interference on sensor performance. Conducting similar experiments with larger motors will provide a more comprehensive understanding of how electromagnetic interference impacts sensors in real-world electric propulsion systems.

In conclusion, while this study has provided valuable insights into the effects of electromagnetic interference on acoustic sensors, it has also highlighted the need for continued research and innovation in this area. By addressing the limitations identified in this study and exploring new avenues for improvement, future research can contribute to the development of more robust and reliable sensor systems for the electric aviation industry. This will be essential to ensuring that the transition to electric propulsion systems does not compromise the ability to accurately monitor and manage noise and vibrations, thereby supporting the broader goals of sustainable and efficient aviation.

# Bibliography

- [1] Guillem Moreno Bravo, Nurgeldy Praliyev, and Árpád Veress. Performance analysis of hybrid electric and distributed propulsion system applied on a light aircraft. *Energy*, 214:118823, 2021. URL: <https://www.sciencedirect.com/science/article/pii/S0360544220319307>, doi:<https://doi.org/10.1016/j.energy.2020.118823>.
- [2] European Commission, Directorate-General for Mobility, Transport, Directorate-General for Research, and Innovation. *Flightpath 2050 – Europe’s vision for aviation – Maintaining global leadership and serving society’s needs*. Publications Office, 2011. doi:[doi/10.2777/50266](https://doi.org/10.2777/50266).
- [3] DLR. EXACT: Project Overview. <https://exact-dlr.de/project-overview/>, 2024.
- [4] Benjamin J. Brelje and Joaquim R.R.A. Martins. Electric, hybrid, and turboelectric fixed-wing aircraft: A review of concepts, models, and design approaches. *Progress in Aerospace Sciences*, 104:1–19, 2019. URL: <https://www.sciencedirect.com/science/article/pii/S0376042118300356>, doi:<https://doi.org/10.1016/j.paerosci.2018.06.004>.
- [5] Bright Appiah Adu-Gyamfi and Clara Good. Electric aviation: A review of concepts and enabling technologies. *Transportation Engineering*, 9:100134, 2022.
- [6] Lothar Bertsch, Mirjam Snellen, Lars Enghardt, and Cornelia Hillenherms. Aircraft noise generation and assessment: executive summary. *CEAS Aeronautical Journal*, 10:3–9, 2019.
- [7] Patxi Gonzalez, Garikoitz Buigues, and Angel Javier Mazon. Noise in electric motors: A comprehensive review. *Energies*, 16(14):5311, 2023.
- [8] Mojtaba Sadeghian. Technologies for aircraft noise reduction: A review. *Journal of Aeronautics & Aerospace Engineering*, 2020.
- [9] Dennis L. Huff, Brenda S. Henderson, and Edmane Envia. A First Look at Electric Motor Noise For Future Propulsion Systems. *Acoustics Technical Working*



- Group Meeting, NASA*, 2016. URL: <https://ntrs.nasa.gov/api/citations/20160014910/downloads/20160014910.pdf>.
- [10] JR Hendershot and BC Kuo. Causes and sources of audible noise in electric motors. In *22nd Incremental Motion Control Systems and Devices Symposium*, pages 259–270, 1993.
- [11] Ali-Mohamed Nassur, Damien Léger, Marie Lefèvre, Maxime Elbaz, Fanny Mietlicki, Philippe Nguyen, Carlos Ribeiro, Matthieu Sineau, Bernard Laumon, and Anne-Sophie Evrard. Effects of aircraft noise exposure on heart rate during sleep in the population living near airports. *International journal of environmental research and public health*, 16(2):269, 2019.
- [12] S Grigg, R Pullin, and CA Featherston. Acoustic emission source location in complex aircraft structures using three closely spaced sensors. *Mechanical Systems and Signal Processing*, 164:108256, 2022.
- [13] EastSensor. Pressure Sensor Noise and EMI, 2024. URL: <https://www.eastsensor.com/blog/pressure-sensor-noise-and-emi/>.
- [14] Clayton R Paul, Robert C Scully, and Mark A Steffka. *Introduction to electromagnetic compatibility*. John Wiley & Sons, 2022.
- [15] KEB America. Introduction to electromagnetic interference with VFDs, 2024. URL: <https://www.kebamerica.com/blog/electromagnetic-interference-vfds/>.
- [16] Norman Violette. *Electromagnetic compatibility handbook*. Springer, 2013.
- [17] Laszlo Tihanyi. *Electromagnetic Compatibility in Power Electronics*, JK Eckert & Company. Inc., Sarasota, Florida, 1995.
- [18] Dr. Gabriel Rojas. Parasitic components in power converters - fundamentals and measurements. URL: <https://www.rohde-schwarz.taipei/data/activity/file/1684810414430757902.pdf>.
- [19] Reinaldo J Perez. *Handbook of Aerospace Electromagnetic Compatibility*. John Wiley & Sons, 2018.
- [20] Yingzhe Wu, Hui Li, Wenjie Ma, Minghai Dong, and Qishui Zhong. High-frequency model of permanent magnet synchronous motor for emi prediction in adjustable speed drive system. In *2018 IEEE International Power Electronics and Application Conference and Exposition (PEAC)*, pages 1–6, 2018. doi:10.1109/PEAC.2018.8590534.

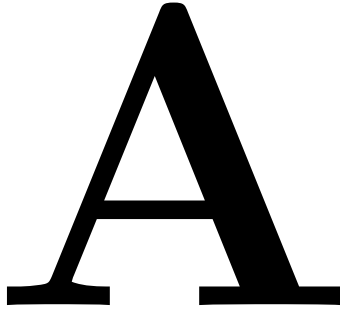
- [21] Praveen Vijayraghavan and R Krishnan. Noise in electric machines: A review. *IEEE Transactions on Industry Applications*, 35(5):1007–1013, 1999.
- [22] Feng Niu, Shiran Cao, Xiaoyan Huang, Jian Zhang, Kui Li, and Youtong Fang. Analysis of emi in motor system driven by pwm inverter. In *2018 1st Workshop on Wide Bandgap Power Devices and Applications in Asia (WiPDA Asia)*, pages 66–70. IEEE, 2018.
- [23] J. Adabi, F. Zare, G. Ledwich, and A. Ghosh. Leakage current and common mode voltage issues in modern ac drive systems. In *2007 Australasian Universities Power Engineering Conference*, pages 1–6, 2007. doi:10.1109/AUPEC.2007.4548097.
- [24] C. Jettanasen. Analysis of conducted electromagnetic interference generated by pwm inverter fed-ac motor drives. In *2012 15th International Conference on Electrical Machines and Systems (ICEMS)*, pages 1–6, 2012.
- [25] Youpeng Huangfu, Shuhong Wang, Luca Di Rienzo, and Jianguo Zhu. Radiated emi modeling and performance analysis of a pwm pmsm drive system based on field-circuit coupled fem. *IEEE Transactions on Magnetics*, 53(11):1–4, 2017. doi:10.1109/TMAG.2017.2705079.
- [26] Signal coupling and cable separation. *Inst Tools*, Jan 2015. URL: <https://instrumentationtools.com/signal-coupling-cable-separation/>.
- [27] J-L Kotny and N. Idir. Time domain models of the emi sources in the variable speed drives. In *2010 IEEE Energy Conversion Congress and Exposition*, pages 1355–1360, 2010. doi:10.1109/ECCE.2010.5618276.
- [28] Phalguni Mathur and Sujith Raman. Electromagnetic interference (EMI): measurement and reduction techniques. *Journal of Electronic Materials*, 49:2975–2998, 2020.
- [29] Reto B Keller. *Design for Electromagnetic Compatibility-In a Nutshell*. Springer, 2023.
- [30] Nick Davis. An introduction to filters. *Allaboutcircuits.com*, Sep 2023. URL: <https://www.allaboutcircuits.com/technical-articles/an-introduction-to-filters/>.
- [31] David Stanis. Selecting the proper emi filter circuit for military and defense applications. *Interference Technology*, Sep 2017. URL: <https://interferencetechnology.com/selecting-proper-emi-filter-circuit-military-defense-applications/>.

- [32] Edvard Csanyi. 9 recommended practices for grounding, Mar 2015. URL: <https://electrical-engineering-portal.com/9-recommended-practices-for-grounding>.
- [33] Thomas F Brooks and William M Humphreys Jr. Flap-edge aeroacoustic measurements and predictions. *Journal of Sound and Vibration*, 261(1):31–74, 2003.
- [34] Martinus P Sanders, Leandro D De Santana, Mahdi Azarpeyvand, and Cornelis H Venner. Unsteady surface pressure measurements on trailing edge serrations based on digital mems microphones. In *2018 AIAA/CEAS Aeroacoustics Conference*, page 3290, 2018.
- [35] Jacob Fraden. Handbook of modern sensors, 1999.
- [36] Stefan Weinzierl. Handbuch der audiotechnik. 2008. URL: <https://api.semanticscholar.org/CorpusID:59660452>.
- [37] My New Microphone. Full List of Microphone Types & Sub-Types, 2024. URL: <https://mynewmicrophone.com/full-list-of-microphone-types-sub-types/>.
- [38] Siti Aisyah Zawawi, Azrul Azlan Hamzah, Burhanuddin Yeop Majlis, and Faisal Mohd-Yasin. A review of mems capacitive microphones. *Micromachines*, 11(5), 2020. URL: <https://www.mdpi.com/2072-666X/11/5/484>, doi:10.3390/mi11050484.
- [39] Youqian Zhang and Kasper Rasmussen. Detection of electromagnetic interference attacks on sensor systems. In *2020 IEEE Symposium on Security and Privacy (SP)*, pages 203–216. IEEE, 2020.
- [40] Denis Foo Kune, John Backes, Shane S Clark, Daniel Kramer, Matthew Reynolds, Kevin Fu, Yongdae Kim, and Wenyuan Xu. Ghost talk: Mitigating emi signal injection attacks against analog sensors. In *2013 IEEE Symposium on Security and Privacy*, pages 145–159. IEEE, 2013.
- [41] Chaouki Kasmi and Jose Lopes Esteves. Iemi threats for information security: Remote command injection on modern smartphones. *IEEE Transactions on Electromagnetic Compatibility*, 57(6):1752–1755, 2015.
- [42] Kommandotech. Condenser vs. Dynamic Microphones, 2024. [Online; accessed 14-August-2024]. URL: <https://kommandotech.com/guides/condenser-vs-dynamic-microphones/>.

- [43] Ashish Kumar, Arathy Varghese, Dheeraj Kalra, Anshuman Raunak, Mahanth Prasad, Vijay Janyani, RP Yadav, et al. Mems-based piezoresistive and capacitive microphones: A review on materials and methods. *Materials Science in Semiconductor Processing*, 169:107879, 2024.
- [44] Benrabeah Djaidir, Mouloud Guemana, Abdallaha Kouzou, and Ahmed Hafaiifa. Failure monitoring of gas turbine based on vibration analysis and detection. In *2017 6th International Conference on Systems and Control (ICSC)*, pages 397–402, 2017. doi:10.1109/ICoSC.2017.7958667.
- [45] Helena Rocha, Christopher Semprimoschnig, and João P. Nunes. Sensors for process and structural health monitoring of aerospace composites: A review. *Engineering Structures*, 237:112231, 2021. URL: <https://www.sciencedirect.com/science/article/pii/S0141029621003813>, doi:<https://doi.org/10.1016/j.engstruct.2021.112231>.
- [46] Diyar Khan and Rafał Burdzik. Measurement and analysis of transport noise and vibration: A review of techniques, case studies, and future directions. *Measurement*, 220:113354, 2023. URL: <https://www.sciencedirect.com/science/article/pii/S0263224123009181>, doi:<https://doi.org/10.1016/j.measurement.2023.113354>.
- [47] Omega Engineering. Accelerometers, 2024. URL: <https://www.omega.com/en-us/resources/accelerometers>.
- [48] Cyril M. Harris, Charles E. Crede, and Horace M. Trent. Shock and vibration handbook. 1976. URL: <https://api.semanticscholar.org/CorpusID:110374775>.
- [49] Sung-Geon Kim, Euibum Lee, Ic-Pyo Hong, and Jong-Gwan Yook. Review of intentional electromagnetic interference on uav sensor modules and experimental study. *Sensors*, 22(6):2384, 2022.
- [50] Mikulas Bittera. Modeling broadband wire antennas with complex geometry. *Procedia Engineering*, 69:1082–1087, 12 2014. doi:10.1016/j.proeng.2014.03.094.
- [51] Grzegorz Lubkowski, Marian Lanzrath, Louis Cesbron Lavau, and Michael Suhrke. Response of the uav sensor system to hpem attacks. In *2020 International Symposium on Electromagnetic Compatibility-EMC EUROPE*, pages 1–6. IEEE, 2020.
- [52] Wade Smith, Zhiqi Fan, Dikang Peng, Zhongxiao Peng, and R.B. Randall. Electromagnetic interference in vibration signals and its effect on bearing diagnostics. 09 2016.

- [53] Wade A. Smith, Zhiqi Fan, Zhongxiao Peng, Huaizhong Li, and Robert B. Randall. Optimised spectral kurtosis for bearing diagnostics under electromagnetic interference. *Mechanical Systems and Signal Processing*, 75:371–394, 2016. URL: <https://www.sciencedirect.com/science/article/pii/S0888327015005993>, doi:<https://doi.org/10.1016/j.ymssp.2015.12.034>.
- [54] Timothy lee lewis, Nikos Nanos, and Christian Málaga-Chuquitaype. Vulnerabilities of low-cost sensors to electro magnetic interference. 09 2022.
- [55] Stephan Elies. Performance analysis of commercial accelerometers: A parameter review. *Sensors & Transducers*, 193(10):179, 2015.
- [56] Paul Cuff. *Lecture 7 ELE 301: Signals and Systems*. 2011. URL: [https://www.princeton.edu/~cuff/ele301/files/lecture7\\_2.pdf](https://www.princeton.edu/~cuff/ele301/files/lecture7_2.pdf).
- [57] Julie Greenberg Bertrand Delgutte. The discrete fourier transform. *Biomedical Signal and Image Processing*, 1999. URL: [https://web.mit.edu/~gari/teaching/6.555/lectures/ch\\_DFT.pdf](https://web.mit.edu/~gari/teaching/6.555/lectures/ch_DFT.pdf).
- [58] Saeed V. Vaseghi. *Advanced Digital Signal Processing and Noise Reduction*. John Wiley & Sons Ltd., 2nd edition, 2000.
- [59] M. Berouti, R. Schwartz, and J. Makhoul. Enhancement of speech corrupted by acoustic noise. In *ICASSP '79. IEEE International Conference on Acoustics, Speech, and Signal Processing*, volume 4, pages 208–211, 1979. doi:[10.1109/ICASSP.1979.1170788](https://doi.org/10.1109/ICASSP.1979.1170788).
- [60] G.R.A.S. GRAS 46BL-1 1/4" CCP Pressure Standard Microphone Set. URL: <https://www.grasacoustics.com/products/measurement-microphone-sets/constant-current-power-ccp-2/product/855-46BL-1>.
- [61] Microtechgefell. Messmikrofon MG 380. URL: <https://www.microtechgefell.de/komplettmessmikrofon?wl=1595-M380#start>.
- [62] Kistler. IEPE Triaxial Accelerometers 8764B. URL: <https://www.kistler.com/INT/en/cp/iepe-triaxial-accelerometers-8764b/P0000561>.
- [63] Huber+Suhner. RG 188 A-U Cable. URL: [https://eu.mouser.com/ProductDetail/HUBER+SUHNER/RG\\_188\\_A-U?qs=byeeYqUIh008zprDYh%2FN8Q%3D%3D](https://eu.mouser.com/ProductDetail/HUBER+SUHNER/RG_188_A-U?qs=byeeYqUIh008zprDYh%2FN8Q%3D%3D).

- [64] Huber+Suhner. RG 174 -U Cable. URL: [https://www.mouser.de/ProductDetail/HUBER+SUHNER/RG\\_174\\_-U?qs=byeeYqUIh00frM8dMG1r4A%3D%3D](https://www.mouser.de/ProductDetail/HUBER+SUHNER/RG_174_-U?qs=byeeYqUIh00frM8dMG1r4A%3D%3D).
- [65] DEWESoft. SIRIUS X. *Data Acquisition-Test and Measurement Solutions*, Jul 2024. URL: <https://dewesoft.com/products/sirius-x>.
- [66] GRAS Sound & Vibration. Gras 42ag sound calibrator, 2024. URL: <https://www.grasacoustics.com/products/calibration-equipment/sound-calibrator/product/756-42ag>.
- [67] Kistler Group. Mobile vibration calibrators 8501a. <https://www.kistler.com/INT/en/cp/mobile-vibration-calibrators-8501a/P0001407>.
- [68] PCB Piezotronics. Understanding sound power and microphone response, 2020. URL: [https://www.pcb.com/Portals/PCB2/Page\\_Teaser/Downloads/TM-AC-PosterBook-dub.pdf?ver=2020-05-28-151358-040](https://www.pcb.com/Portals/PCB2/Page_Teaser/Downloads/TM-AC-PosterBook-dub.pdf?ver=2020-05-28-151358-040).
- [69] Sengpiel Audio. Sound and distance calculator, 2024. URL: <https://sengpielaudio.com/calculator-SoundAndDistance.htm>.
- [70] PIC Wire & Cable. Velocity factor in cables. Technical report, n.d. URL: [https://www.picwire.com/Files/Technical-Articles/Velocity-Factor\\_PIC\\_Technical-Article.pdf](https://www.picwire.com/Files/Technical-Articles/Velocity-Factor_PIC_Technical-Article.pdf).
- [71] Analog Devices. Folded frequency calculator, n.d. URL: <https://www.analog.com/en/resources/design-notes/foldedfrequency-calculator.html>.



## Code Snippets

```
1 from scipy.signal import welch
2 P_ref = 2e-5
3 # Function to plot PSD and highlight maximum PSD value
4 def plot_psd(ax, signal1, signal2, signal3, xlim):
5     # Compute PSD for the first microphone
6     freq_noisy, psd_noisy = welch(signal1, fs=sampling_rate, nperseg=2048,
7     noverlap=1024)
8     psd_dB_noisy = 10 * np.log10((psd_noisy) / (P_ref**2))
9
10    freq_noise, psd_noise = welch(signal2, fs=sampling_rate, nperseg=2048,
11    noverlap=1024)
12    psd_dB_noise = 10 * np.log10((psd_noise) / (P_ref**2))
13    avg_psd_noise = np.mean(psd_dB_noise)
14
15    enhanced_signal = (psd_dB_noisy - avg_psd_noise)
16
17    freq_clean, psd_clean = welch(signal3, fs=sampling_rate, nperseg=1024,
18    noverlap=712)
19    psd_dB_clean = 10 * np.log10((psd_clean) / (P_ref**2))
20
21    # Plot PSD for the first microphone
22    ax.plot(freq_noisy, enhanced_signal, linewidth=2, color='crimson',
23    label='Estimated')
24
25    # Plot PSD for the second microphone
26    ax.plot(freq_clean, psd_dB_clean, linewidth=2, color='darkgreen',
27    label='Original')
```